Geophysical Journal International

Geophys. J. Int. (2018) **214,** 1441–1466
Advance Access publication 2018 May 28
GJI Marine geosciences and applied geophysics

doi: 10.1093/gji/ggy218

Field-scale comparison of frequency- and time-domain spectral induced polarization

P.K. Maurya, G. Fiandaca, A.V. Christiansen and E. Auken

HydroGeophysics Group, Department of Geoscience, Aarhus University, C.F. Møllers Alle 4, 8000 *Aarhus C, Denmark. E-mail: pradip.maurya@geo.au.dk*

Accepted 2018 May 26. Received 2018 May 24; in original form 2018 April 11

SUMMARY

In this paper we present a comparison study of the time-domain (TD) and frequency-domain (FD) spectral induced polarization (IP) methods in terms of acquisition time, data quality and spectral information retrieved from inversion. We collected TDIP and FDIP surface measurements on three profiles with identical electrode setups at two different field sites with different lithology. In addition, TDIP data were collected in two boreholes using the El-Log drilling technique in which apparent formation resistivity and chargeability values are measured during drilling using electrodes integrated within the stem auger.

The TD and FD data were processed and inverted with similar approaches. The IP voltage decays and complex impedance spectra were inspected quadrupole by quadrupole for outliers. In the inversion, the apparent resistivity values and the full IP decays (in TD) or the full complex impedance spectra (in FD) for all quadrupoles were inverted simultaneously in 2-D using a modified parametrization of the Cole-Cole model. Furthermore, inversions of synthetic models mimicking the field situations were performed. The comparisons reveal that TD and FD results are comparable not only qualitatively, but also quantitatively. Furthermore, the surface inversions are in agreement with the borehole results and lithology, within the resolution capability of the surface measurements. In particular, comparable spectral IP parameters were retrieved for both sites with both measurement approaches, with relaxation times between 10^{-2} s and 1 s, suggesting a spectral coverage at least up to 100 Hz for both TD and FD measurements. However, for the employed data acquisition procedures and instrumentations, the TD measurements had an advantage in terms of acquisition speed and usable spectral acquisition range compared to the FD measurements. We conclude that the TD method, as the FD method, is a suitable tool to recover spectral IP information in the field, provided that the measurement procedures are planned accordingly and the subsurface IP response is in the spectral range covered by the measurements.

Key words: Electrical properties; Hydrogeophysics; Inverse theory; Tomography.

INTRODUCTION

From an early stage of its development to present-day, the induced polarization (IP) method has been a popular choice among the ground based geophysical methods for mineral exploration (Marshall & Madden 1959; Wong 1979; Seigel *et al.* 2007). However, during the last two decades IP has been used increasingly for hydrogeological and environmental investigations in the field, for example, for lithological discrimination (Slater & Glaser 2003; Hördt *et al.* 2009; Gazoty *et al.* 2012b; Chongo *et al.* 2015; Johansson *et al.* 2016; Maurya *et al.* 2018), landfill delineation (Gazoty *et al.* 2012a; Wemegah *et al.* 2017) and characterization of contaminated sites (Kemna *et al.* 2004; Flores Orozco *et al.* 2012; Johansson *et al.* 2015).

The spectral information contained in the IP data, that is, the characteristic frequency dependence of the IP response, has been investigated in detail for near-surface imaging purposes, both in frequency-domain (FD) IP and time-domain (TD) IP as summarized by Kemna *et al.* (2012). For low current densities, the IP phenomenon is linear (Komarov 1980) and the FDIP and TDIP responses are related to each other through the Fourier Transform (Shuey & Johnson 1973). However, the FD and TD methods are completely equivalent only under the assumption of the absence of noise and infinite acquisition range (i.e. frequencies going to infinite and, in a logarithmic sense, times going to zero). Consequently, the IP spectral content actually retrievable from FD and TD data may differ significantly, for both laboratory and field data, simply because of the different data noise and measurable acquisition ranges.

Differences may also arise from the acquisition procedures, the used instrumentations and the inversion schemes. In this respect, both methods have become more robust and effective following significant advancements in hardware, data acquisition techniques and inversion algorithms. Multielectrode and multichannel IP instruments for fast and accurate data acquisition for both TD and FD are available, as well as accurate forward and inversion algorithms.

In the FD, Kemna *et al.* (2000) developed a complex inversion scheme for single-frequency inversion problems and fitted the resulting spectra, extracted from independent inversions for all frequencies, for each model cell in terms of the Cole-Cole model (Pelton *et al.* 1978b). Loke *et al.* (2006) inverted the FD data of all frequencies at once with a two-step approach: first, the initial resistivity and chargeability models were computed through an approximate inversion method; and second, the full Cole-Cole parameters were retrieved following the approach developed by Routh *et al.* (1998). The FD data at all frequencies were inverted simultaneously in the inversion scheme presented by Kemna *et al.* (2014) and Günther & Martin (2016). In this case, the complex conductivity values were modelled in each inversion cell and smoothness constraints were applied between the conductivity values of adjacent frequencies.

TDIP imaging inversion schemes were initially restricted to total chargeability estimation (Oldenburg & Li 1994), thus discarding the spectral information present in the full-decay curves. Attempts of spectral inversion were made by inverting the time gates independently using a direct current (DC) resistivity algorithm, and fitting the resulting time-dependent resistivity in terms of Cole-Cole parameters (Yuval & Oldenburg 1997; Hördt *et al.* 2006; Hönig & Tezkan 2007). However, these algorithms had not taken the transmitter waveform in the forward computations into account, limiting their ability to resolve the spectral information from the IP decays quantitatively. Furthermore, the retrieved time-dependent resistivity series did not necessarily obey the physics of the problem, because the different noise levels and the resolution of the independent DC inversions may result in unrealistic decays. On the contrary, Fiandaca *et al.* (2012, 2013) developed TD 1-D and 2-D inversion algorithms that invert the full IP decays simultaneously, with an accurate description of transmitter waveform and receiver transfer function, for resolving the spectral information quantitatively. Madsen *et al.* (2017b) showed through 1-D Markov Chain Monte Carlo (MCMC) inversions that the Cole-Cole parameters can be resolved from full-decay TDIP data if an appropriate acquisition range above two decades in time is applied, and that strong parameter correlations exist when small values of the frequency exponent C are modelled. Furthermore, Madsen *et al.* (2017a) presented how the full-decay IP inversion in terms of Cole-Cole parameters helps in overcoming well-known resistivity equivalences.

The spectral IP method has been applied successfully at field scale for spectral imaging in the FD (Kemna *et al.* 2004; Orozco *et al.* 2012; Attwa & Günther 2013; Orozco *et al.* 2013) and in the TD (Gazoty *et al.* 2012a,b; Doetsch *et al.* 2015a,b; Fiandaca *et al.* 2015b; Johansson *et al.* 2015; Johansson *et al.* 2016; Wemegah *et al.* 2017). Attempts have been made to compare the FD and TD spectral responses (Zonge *et al.* 1972; Johnson 1984); however, a comparison of spectral imaging capabilities of both methods based on tomographic inversion has not been presented so far.

We present a comprehensive field survey comparison of the FD and TD methods, in terms of acquisition time, data quality, as well as spectral information retrieved from the inversion. We collected FD and TD spectral IP measurements on three profiles at two different field sites in Denmark with an identical electrode setup and comparable frequency/time acquisition ranges. Each measured signature (impedance spectrum or decay curve) was individually analysed in the outlier removal process. Afterwards, identical 2-D inversion procedures were used (the only differences being the data space and the forward computation) in order to minimize inversion-related differences in the FD and TD inverted spectral content. In particular, the full spectra (in FD) and full decays and apparent resistivity values (in TD) were inverted simultaneously in terms of a re-parametrization of the Cole-Cole model (Fiandaca *et al.* 2018). Actually, the 2-D FD inversion scheme used in this study has been developed specifically for this comparison, and consistent inversion behaviour is assessed by means of numerical simulations in both the TD and the FD, using a synthetic model mimicking the field conditions. Furthermore, TDIP data were acquired *in situ* in two boreholes close to one of the measured profiles and subsequently inverted in 1-D for comparison with the surface results.

MATERIALS AND METHODS

Spectral IP method

In the IP method, the low-frequency polarization properties of the Earth are measured as a frequency-dependent complex impedance (in FD) or a voltage decay response (in TD) when the medium is excited by a time-varying electric current. Measurements in the FD are conducted by applying a time-variable sinusoidal voltage at the current injection dipole, and measuring the resulting injection current as well as potential differences at one or more dipoles located along the measurement profile. The resulting complex impedance can be presented as a magnitude and a phase shift. The phase shift is the phase lag between the injected current and the measured voltage signal. Spectral signatures are recorded by subsequently applying different frequencies. Taking the measurement geometry into account, FD spectral IP measurements can be expressed in terms of apparent complex conductivity σ^* or its inverse, apparent complex resistivity ρ^*, as real and imaginary components or amplitude and phase (e.g. Slater & Lesmes 2002):

$$\sigma^*(f) = |\sigma^*(f)|\ e^{i\varphi(f)} = \sigma'(f) + i\sigma''(f) \tag{1a}$$

$$\rho^*(f) = |\rho^*(f)|\ e^{-i\varphi(f)} = \rho'(f) + i\rho''(f) \tag{1b}$$

with i being the imaginary unit, f (Hz) the frequency, and φ (mrad) the frequency-dependent phase (here of complex conductivity), and $'$ and $''$ denoting real and imaginary components, respectively.

In TD, the IP effect is measured using square current pulses, where either the voltage rise (100 per cent duty cycle) or the voltage decay (50 per cent duty cycle) is recorded during the current on-time or off-time, respectively (Olsson *et al.* 2015). In a 50 per cent duty cycle measurement, current is turned on for a finite time and after a charge-up effect, the primary voltage (V_{dc}) is measured for the computation of the direct-current (DC) resistivity, just before the current is turned off. After the current is turned off, the voltage drops to a secondary level and then decays with time, which represents the target of TDIP (Gazoty *et al.* 2013). In 100 per cent duty cycle measurements, the (increasing) voltage is measured during the on-time and the corresponding IP decay curve is obtained as described in Olsson *et al.* (2015):

$$V_{ip}(t) = V_{dc} - V_{measured}(t), \tag{2}$$

where V_{ip}(Volt) is the decay voltage signal at time t (analogous to 50 per cent decay), V_{dc} (Volt) is the DC voltage measured at the end of the current pulse (where the voltage reaches maximum level) and

V_{measured} (Volt) is the measured signal at time t during the acquisition. Olsson *et al.* (2015) have shown that the spectral information obtained from both types of measurements is equivalent, but the 100 per cent duty cycle approach is twice as fast as the 50 per cent approach, and the signal level is almost doubled.

Because of electromagnetic (EM) induction effects occurring just after the current switch, a time gap or delay is applied before performing the TDIP measurements (typically 1–20 ms). The signal decay is usually integrated over n logarithmically spaced time windows (or gates) for the computation of the apparent chargeability M:

$$M_i = \frac{1}{V_{\text{dc}}\,(t_{i+1} - t_i)} \int_{t_i}^{t_{i+1}} V_{\text{ip}} \mathrm{d}t, \tag{3}$$

where t_i and t_{i+1} are the opening and closing times for the gate over which the signal is integrated and M_i is usually expressed in mV V^{-1}.

The amplitude and phase spectra of the complex resistivity FD measurements (eq. 1b) and the TD apparent resistivity values and decays (eq. 3) for each quadrupolar measurement represent the FD and TD data sets used in this study.

Electromagnetic effects in spectral IP

While the capacitive properties of the subsurface are the target of the IP method, the injection of alternating currents and the current switch generate also EM inductive effects, which can be described in the general form of the mutual impedance between the 'current' and 'potential' circuits (Sunde 1968). Furthermore, capacitive coupling exists between the ground and the receiver wires (Zonge & Hughes 1985; Ingeman-Nielsen 2006) and between current/potential wires in multichannel cables (Dahlin & Leroux 2012), which superposes as well to the IP signal. These effects are generally referred to as inductive and capacitive coupling, respectively, and are more severe at high frequencies/early times. Inductive coupling is unavoidable, depends on the cable layout (Sunde 1968) and affects the IP data more severely on conductive, weakly chargeable media (Dey & Morrison 1973). Capacitive coupling depends on the distributed wire-to-ground and wire-to-wire capacitance and on the contact resistance (Ingeman-Nielsen 2006; Dahlin & Leroux 2012), and its strength in relation to the IP signal can be diminished by decreasing the contact resistance.

In this study inductive and capacitive EM effects are not modelled, and data interpreted as affected by coupling are culled out before inversion. For this reason, it is important to understand the extent of the EM effects and in particular of the unavoidable EM induction. EM induction has been treated in several studies (Dey & Morrison 1973). Fiandaca (2018) presents a comparison of the spectral FD and TD methods specifically with a view to evaluating the induction-free acquisition ranges (i.e. the ranges where the induction is negligible in comparison to the IP galvanic response), for nested and non-nested electrode arrays. Fig. 1, extracted from Fiandaca (2018), presents a comparison of EM and IP phase spectra and decays for a constant phase angle (CPA) IP model (Van Voorhis *et al.* 1973) over a homogeneous half-space. According to Fiandaca (2018), for the gradient array it is typically possible to measure less than two/one decades of induction-free data in FD, while more than four decades in TD (when using 3 m or more for the potential dipole length and lower frequencies down to a few tens of mHz, as in this study). Fiandaca (2018) shows also that dipole–dipole FDIP measurements are less affected by inductive coupling, but while the coupling decreases with the dipole order, the IP signal level decreases quicker, leading to an increased EM effect on the IP data. Contrarily than in FD, in TD the dipole–dipole array is worse than nested arrays in terms of induction-free acquisition range.

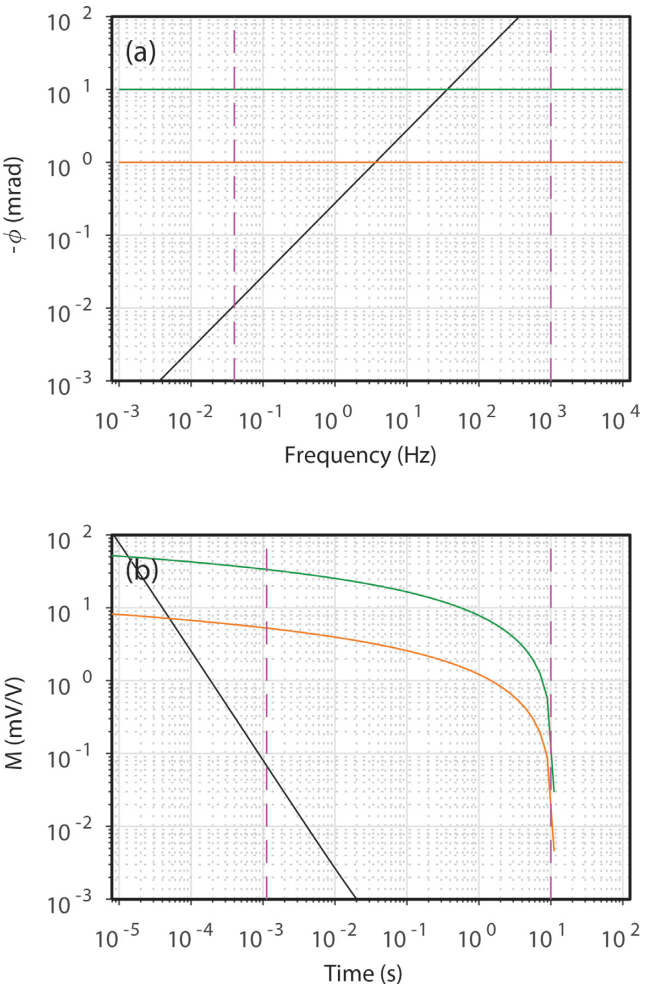

Figure 1. Modified from Fiandaca (2018). (a) Comparison of EM and IP phase spectra and (b) Comparison of EM and IP decays. Continuous black lines: EM phase spectrum/decay of a gradient array, for $\rho = 25$ Ωm. Green and orange lines: CPA phase spectra/decays for $\varphi = -10$ mrad and $\varphi = -1$ mrad, respectively. Magenta dashed lines: minimum/maximum frequency/time measured in this study. The gradient array is defined as MN = 3 m, AB = 9 · MN, $\frac{\text{AM}}{\text{MN}} = 4$ and $d = 0.002$ m, where d is the distance between the current and voltage lines.

Study area

To compare the FD and TD methods in different geological settings we selected two landfill sites, one located at Grindsted and one at Pillemark (on the island of Samsø, as shown in Fig. 2). At Grindsted, the deposited waste in the landfill consists of municipal solid waste, industrial waste, sewage treatment waste and demolition waste. Since there is no leachate collection or liner beneath the landfill, the leachate plume originated from the landfill migrates in a northwest direction, following the groundwater flow (Kjeldsen *et al.* 1998; Maurya *et al.* 2017). Quaternary sand deposits on top of a micaceous tertiary sand formation mostly dominate the geology of the Grindsted area. Thin clay-lignite layers are present in the micaceous sand unit.

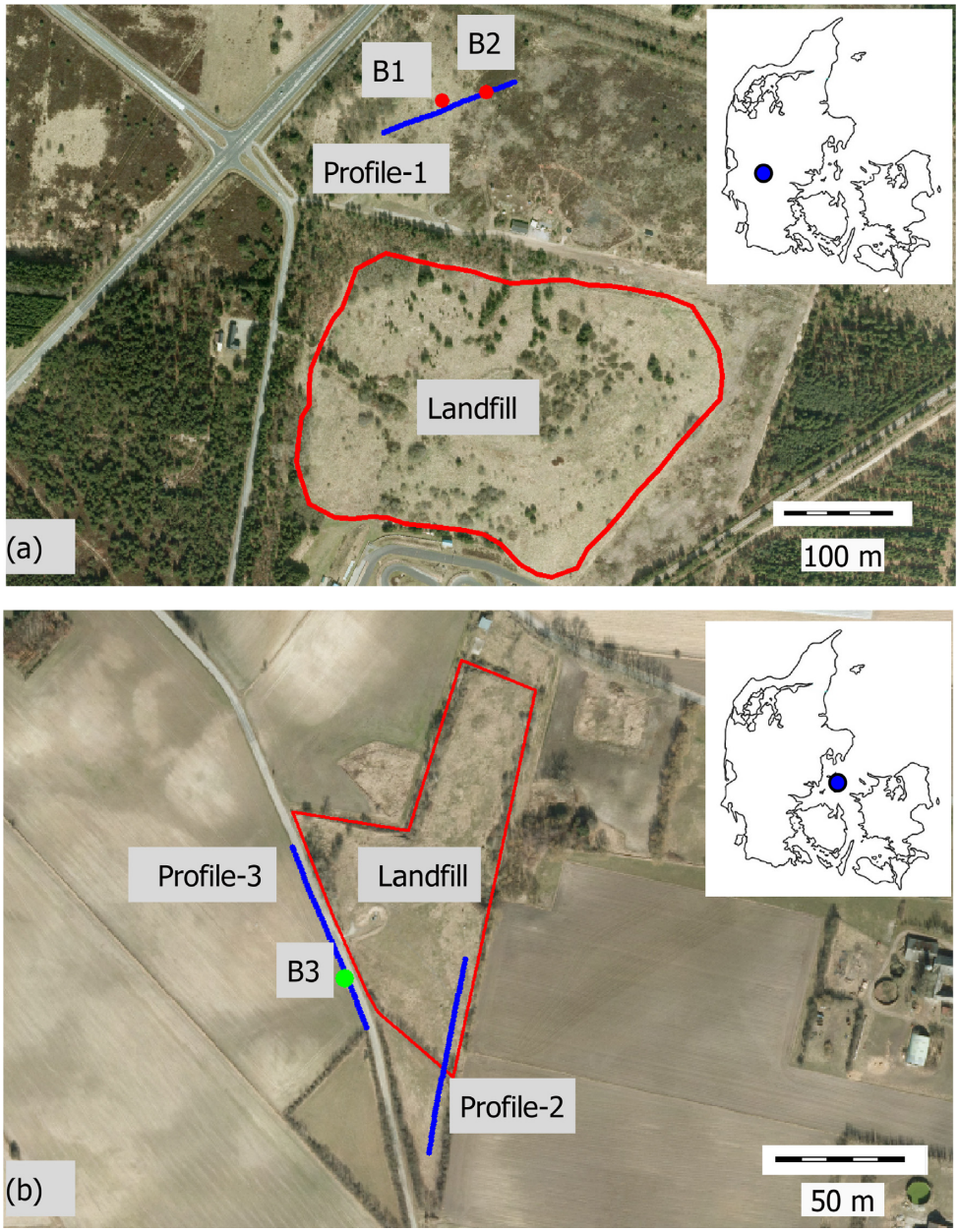

Figure 2. Maps of the field sites and location of the profiles. (a) Grindsted. (b) Pillemark. Blue lines represent the profiles and red dots are the positions of the El-logs. Green dots are lithological logs. Landfill's boundaries are marked in red.

The geology of the Pillemark area is more complex than the geology at Grindsted, and is very heterogeneous in the top 10–12 m, characterized by late-glacial meltwater deposits and post-glacial freshwater sand and peat. Below that, a clay-till layer approximately 20 m thick is present, followed by a regional aquifer in meltwater sand and gravel deposits. The deposited waste in the Pillemark landfill consists of sewage sludge, household waste and industrial waste, and no leachate protection is present.

Fig. 2 shows the location of three profiles collected in this study. Profile 1 was collected outside the Grindsted landfill area oriented approximately perpendicularly to the groundwater flow direction (NW). Profiles 2 and 3 were collected at Pillemark, crossing over the landfill and just outside it, respectively.

Data acquisition and processing

All data profiles (Fig. 2) were collected using 49 electrodes with 3 m spacing, for a total length of 144 m. The TD data were acquired using the ABEM Terrameter-LS instrument (www.guidelinegeo.com) and FD data were measured using the Radic SIP256c instrument (www.radic-research.de). For profile 1 both gradient (GR) and dipole–dipole (DD) array configurations were measured with TD and FD data, whereas for profiles 2 and 3 gradient data were acquired only for TD. The dipole–dipole FD acquisition had no technical limit in the maximum dipole order of the sequence, because the Radic SIP256c can measure all the voltages between consecutive electrodes for each current injection (but measurements with poor signal-to-noise ratio were culled out in the processing), while it was

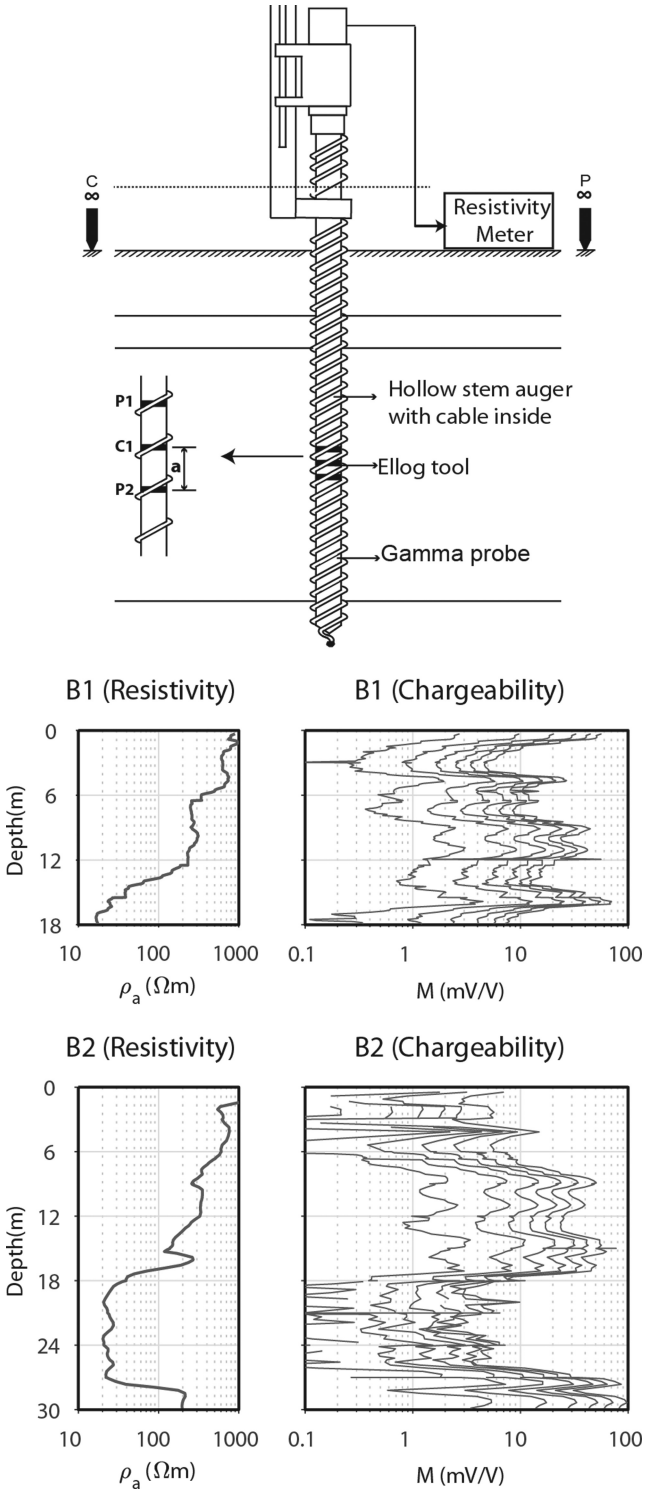

Figure 3. Sketch of the El-log system (top). Resistivity and TD chargeability data from B1 (middle) and B2 El-log measurements (bottom). The chargeability data are shown every sixth gate.

decided to limit the maximum order of the dipole–dipole TD acquisition to 7, matching the multichannel capability of the Terrameter-LS instrument. The TD and FD acquisition settings were selected in order to obtain a comparable spectral range, with a time range of the voltage decays from 10^{-3} s to 12 s and a frequency range of the complex impedance spectra from 4×10^{-2} to 10^3 Hz. All details on the acquisition parameters and array settings are stated in Tables 1 and 2.

When measuring the TDIP data the electrodes were wetted with salty water in order to decrease the contact resistance at the electrodes and consequently the capacitive coupling between individual current and potential wires. Furthermore, both dual-spread (separate current and potential cables) and single-spread cable layouts were employed, in order to verify the presence of capacitive/inductive coupling in the data due to cable interference (Dahlin & Leroux 2012). For the FD acquisition direct and reciprocal measurements were carried out in profile 2, for a better estimate of the data repeatability.

Data in both domains were processed in a similar manner for removing bad quality decays/spectra. However, an additional step was taken in TD, where the full-waveform data acquired at a 3750 Hz sampling rate were pre-processed for harmonic denoising and background drift removal, following Olsson *et al.* (2016). After applying the harmonic denoising and the background removal, the full-waveform TD data were gated using 41 logarithmically spaced gates from 10^{-3} to 12 s. This pre-processing step increases the overall usable time range of the IP decays significantly and is extremely important for extracting the spectral information of the TDIP data.

The denoised and regated TDIP data were imported to the Aarhus Workbench software (www.aarhusgeosoftware.dk) for manual processing of IP decays. Single gates or entire decays showing EM coupling or poor quality, for instance due to poor signal-to-noise ratio, were removed.

A similar approach was adopted for FD data processing. Both normal and reciprocal dipole–dipole data were imported into Aarhus Workbench and a detailed manual inspection of amplitude and phase spectra was performed.

In addition to the surface measurements, we acquired TDIP data in two boreholes at Grindsted using the El-Log drilling technique (Gazoty *et al.* 2012a). The positions of the boreholes (B1 and B2) are shown in Fig. 2.

With the El-log method, apparent formation resistivity and chargeability values are measured during drilling using electrodes integrated within the hollow stem auger. The electrodes are embedded in insulating material and are connected through the cables to the resistivity metre on the ground. The instrument was the same as used for surface measurements. The Pole–Pole array was used for these measurements, with two electrodes C_∞ and P_∞ placed on the surface as remote current and potential electrodes, and one current electrode C_1 and two potential electrodes P_1 and P_2 embedded in the auger (two potential electrodes P_1 and P_2 for measuring two channels at once with reference to P_∞). Fig. 3 shows a sketch of the El-log acquisition system and the recorded apparent resistivity and chargeability data for the B1 and B2 El-logs. The acquisition settings are shown in Table 1. The same processing as applied to the surface TDIP data was carried out on the El-log TDIP data.

Spectral inversion of IP data

For the spectral inversion of the IP data, we used the AarhusInv code (Auken *et al.* 2015). Prior to this study, the code supported 1-D and 2-D inversion of TDIP data (Fiandaca *et al.* 2012; Fiandaca *et al.* 2013), in which the apparent resistivity values and the full IP decays are inverted simultaneously for Cole–Cole model parameters, with an accurate description of transmitter waveform and receiver transfer function. In order to avoid any bias in the comparison due to the use of different inversion approaches for TD and FD data, a

Table 1. Acquisition information.

	Method		
	Surface TDIP	Surface FDIP	Borehole TDIP
Instrument	ABEM Terrameter LS	Radic SIP256c	ABEM Terrameter LS
Sampling rate	3750 Hz	up to 1600 Hz	3750 Hz
Waveform	Square wave 100 per cent duty cycle	Sinusoidal	50 per cent duty cycle
Acquisition range	0.001–12 s	0.04–1000 Hz	0.001–4 s
Points per decade	10	4	10
Stack size	2	2	1

Table 2. Quadrupolar measurement sequences for gradient (GR) and dipole–dipole (DD) arrays.

Array type	GR Gradient	DD 7 orders Dipole–dipole	DD all orders, A Dipole–dipole	DD all orders, B Dipole–dipole	DD all orders, C Dipole–dipole
No. electrodes	49	49	49	49	49
Electrode spacing	3 m	3 m	3 m	3 m	3 m
No. quadrupoles	735	433	1377	2382	1081
No. current injections	105	80	80	160	46
Settings	$\|MN\| = 3,6,9m$ $\|AB\| = 9\|MN\|$	$\|BN\| = 7\|AB\|$ $\|AB\| = 3$, 12 m	$\|BN\| \leq 46\|AB\|$ $\|AB\| = 3$, 12 m	$\|BN\| \leq 46\|AB\|$ $\|AB\| = 3$, 12 m + reciprocals	$\|BN\| \leq 46\|AB\|$ $\|AB\| = 3$ m
Average geometrical factor after processing (DC/Amplitude data)	335 m	2389 m	18 576 m	30 358 m	36 530 m
Average geometrical factor after processing (Decay/Phase data)	333 m	1838 m	1749 m	2547 m	4133 m

The 'Settings' row in the table describes the used sequences, in terms of length of the current and potential dipoles |AB| and |MN|, and relations between |AB| and |MN|.

Table 3. Comparison of acquisition times for sequences described in Table 2.

	Method	
	TDIP	FDIP
Measure acquisition time per current injection	55 s	522 s
Theoretical acquisition time per current injection	48	102
Sequence acquisition time, GR	1.5 hr	11.7 hr
Sequence acquisition time, DD 7 orders	1.2 hr	11.6 hr
Sequence acquisition time, DD all orders B (with reciprocals)	2.4 hr	23.2 hr

new FDIP forward response was implemented in AarhusInv. Similar to the TDIP inversion, for each quadrupole the amplitudes and phases at all frequencies are inverted simultaneously in the inversion process.

The model space is a reparametrization of the Cole–Cole model, namely the maximum phase angle (MPA) Cole–Cole model (Fiandaca *et al.* 2017; Fiandaca *et al.* 2018). In the Cole–Cole model, as defined by (Pelton *et al.* 1978b), the complex resistivity ρ^* as a function of frequency f is defined as

$$\rho^*(f) = \rho_0 \left[1 - m_0 \left(1 - \frac{1}{1 + (i2\pi f \tau_\rho)^C} \right) \right], \tag{4}$$

where ρ_0 is the direct-current resistivity, m_0 is the intrinsic chargeability, τ_ρ is the characteristic relaxation time, C is the frequency exponent and i is the imaginary unit.

In the MPA Cole–Cole model, the maximum phase shift $\varphi_{\max}$ (defined as phase of the complex conductivity to enforce positivity in the inversion) and the time constant τ_φ (i.e. the inverse of the angular frequency at which $\varphi_{\max}$ is reached, see Fig. 4) are used instead of m_0 and τ_ρ as inversion parameters. This is because the parameters $\{\rho_0, \varphi_{\max}, \tau_\varphi, C\}$ are significantly better resolved than $\{\rho_0, m_0, \tau_\rho, C\}$, both in FD and TD spectral IP inversion, as shown through the Markov Chain Monte Carlo (MCMC) inversion approach in Fiandaca *et al.* (2017) and Fiandaca *et al.* (2018).

The MPA parameters are defined in each cell (i, j) of the 2-D model grid and the FD forward response and Jacobian are computed solving the Poisson's equation, Fourier transformed in the strike direction, through the finite-element method (Fiandaca *et al.* 2013). The FD Jacobian elements with respect to the MPA parameters are computed through the chain rule:

$$\frac{\partial F^*_{\mathrm{FD}}}{\partial p_n} = \frac{\partial F^*_{\mathrm{FD}}}{\partial \sigma^*} \cdot \frac{\partial \sigma^*}{\partial p_n}, \tag{5}$$

where $\frac{\partial F^*_{\mathrm{FD}}}{\partial \sigma^*}$ is computed (Kenkel & Kemna 2017) by the adjoint method and $\frac{\partial \sigma^*}{\partial p_n}$ is computed numerically for each MPA parameter p_n. The forward response and the Jacobian for the TD inversion are obtained through superposition of step responses computed by the fast Hankel transform as described in (Johansen & Sørensen 1979; Fiandaca *et al.* 2013). For the inversion of the TDIP El-log data, the forward response is computed in 1-D following Fiandaca

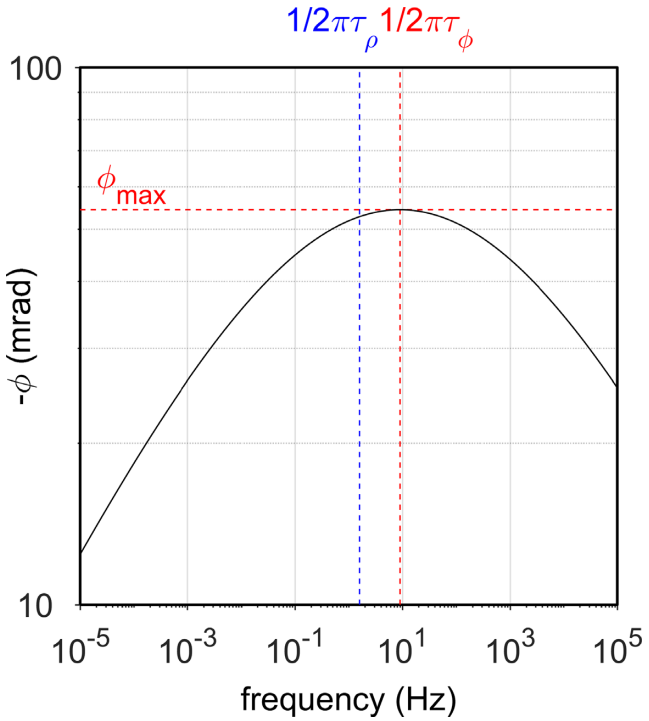

Figure 4. Phase spectrum of the Cole-Cole model (black line) and the new MPA inversion parameters φ_{max} and τ_φ (in red). In blue, the classic relaxation time τ_ρ of the resistive Cole-Cole formula (eq. 4).

et al. (2012) but using an FD kernel that allows buried electrodes as described in Sato (2000).

The inversion process is carried out iteratively as described in Auken *et al.* (2015), with the objective function Q and the model update $\boldsymbol{m}_{(n+1)}$ given as:

$$Q = \left(\frac{\left[\delta \boldsymbol{d}'^{T} \boldsymbol{C}'^{-1} \delta \boldsymbol{d}' \right]}{N_d + N_r} \right)^{1/2} \tag{6}$$

$$\boldsymbol{m}_{(n+1)} = \boldsymbol{m}_{(n)} + \left[\boldsymbol{G}'^{T}_{(n)} \boldsymbol{C}'^{-1} \boldsymbol{G}'_{(n)} + \lambda_{(n)} \boldsymbol{I} \right]^{-1} \cdot \left[\boldsymbol{G}'^{T}_{(n)} \boldsymbol{C}'^{-1} \delta \boldsymbol{d}' \right], \tag{7}$$

where N_d and N_r are the number of data points and the number of roughness constraints, $\lambda_{(n)}$ is the iteratively updated damping parameter and the Jacobian $\boldsymbol{G}'_{(n)}$, the covariance matrix $\boldsymbol{C}'$ and the data residual vector $\delta \boldsymbol{d}'$ are defined as

$$\boldsymbol{C}' = \begin{bmatrix} \boldsymbol{C}_{\text{obs}} & 0 \\ 0 & \boldsymbol{C}_R \end{bmatrix} \tag{8}$$

$$\delta \boldsymbol{d}' = \begin{bmatrix} \boldsymbol{d}_n - \boldsymbol{d}_{\text{obs}} \\ -\boldsymbol{R}\boldsymbol{m}_n \end{bmatrix} \tag{9}$$

$$\boldsymbol{G}'_{(n)} = \begin{bmatrix} \boldsymbol{G}_{(n)} \\ \boldsymbol{R} \end{bmatrix}, \tag{10}$$

where $\boldsymbol{C}_{\text{obs}}$ and $\boldsymbol{C}_R$ are the covariance matrices of the data and of the roughness constraints, respectively; $\boldsymbol{d}_{\text{obs}}$ and $\boldsymbol{d}_n$ represent the data vector and the forward response of the model vector $\boldsymbol{m}_n$ at the nth iteration; $\boldsymbol{R}$ is the roughness matrix and $\boldsymbol{R}\boldsymbol{m}_n$ represents the roughness of the model vector $\boldsymbol{m}_n$; $\boldsymbol{G}_{(n)}$ is the Jacobian of the forward mapping.

In the FD inversion the phase and amplitude data for each quadrupolar measurement are treated as independent data, and the Jacobian $\boldsymbol{G}_{(n)}$ is real valued (as in the TD inversion). In both TD and FD inversions a logarithmic transformation is applied to the model parameters, while the data are kept in linear space because negative data are measured. The use of the logarithm of all the parameters in the inversion algorithm has not been guided by physical considerations, but is a pragmatic solution because our algorithm allows the log transformation on all the parameters or none.

In Fiandaca *et al.* (2013) and Auken *et al.* (2015), all the inversion parameters are damped through the maximum diagonal element of the matrix $\boldsymbol{G}'^{T}_{(n)} \boldsymbol{C}'^{-1} \boldsymbol{G}'_{(n)}$. This damping scheme may overdamp the weakly resolved parameter types, like the relaxation time τ_φ, limiting their variation through the inversion process. For this reason, in this study the damping parameter $\lambda_{(n)}$ of eq. (7) is computed differently for each type of the inversion parameters $\{\rho_0,\ \varphi_{\max}, \tau_\varphi, C\}$, through the four maximum diagonal elements of the matrix $\boldsymbol{G}'^{T}_{(n)} \boldsymbol{C}'^{-1} \boldsymbol{G}'_{(n)}$ of each parameter type.

Alongside the inversion results, the depth of investigation (DOI) of the inversion model is presented. The DOI algorithm used in this study is based on a Cumulated Approximated covariance Analysis (CAA) that incorporates both the Jacobian $\boldsymbol{G}_{(n)}$ of the actual inversion model $\boldsymbol{m}_n$ (cumulated over the model layers) and the data covariance $\boldsymbol{C}_{\text{obs}}$, as described in Fiandaca *et al.* (2015a). Considering that the Jacobian $\boldsymbol{G}_{(n)}$ depends on the four parameter types $\{\rho_0,\ \varphi_{\max}, \tau_\varphi, C\}$, a different DOI estimate is retrieved for each parameter type, with lower values for the weakly resolved parameters.

For a given depth D, the CAA computes the data-based cumulated uncertainty analysis $[\boldsymbol{G}^{T}_{\text{cum}} \boldsymbol{C}^{-1}_{\text{obs}} \boldsymbol{G}_{\text{cum}}]^{-1}$, model column by model column. This is done by cumulating the sensitivity $\boldsymbol{G}_{(n)}$ of all the model cells below the depth D into the cumulated $\boldsymbol{G}_{\text{cum}}$. A threshold value for the CAA is defined, and the DOI is computed as the depth at which this threshold is reached. Based on experience, DOI threshold values between 2 and 5 give reasonable DOI estimations. Usually larger values of the DOI threshold are used for the τ_φ parameter, which is significantly less resolved and for which the order of magnitude is of interest even when the parameter resolution is low. In this study, two DOI thresholds are used: a more conservative threshold equal to 2 and a less conservative threshold equal to 5. For the τ_φ parameter the thresholds are increased by a factor of 5.

COMPARISON OF ACQUISITION TIME AND DATA QUALITY

Table 3 shows a comparison of the acquisition time per current injection and per sequence for the acquisition settings used in this study (see Tables 1 and 2): the TD acquisition is approximately 10 times faster than the FD acquisition, despite the low-frequency spectral content of the TD/FD acquisitions being similar. In fact, the period of the TD current injection is 24 s (twice the current on-time), while the period of the smallest FD frequency is 25 s. With 4 points per decade in the FD acquisition and two stacks, as used in this study, the theoretical minimum FD acquisition time per current injection is only 102 s (the sum of the periods of all the measured frequencies, multiplied by two because of the stacking), instead of the 522 s actually spent in the field. On the contrary, the theoretical minimum TD acquisition time per current injection is 48 s, compared to the 55 s spent in the field. The difference between the theoretical and measured FD acquisition time depends on the instrument used, and is probably due to the data transfer time between the distributed measurement units and the central instrument.

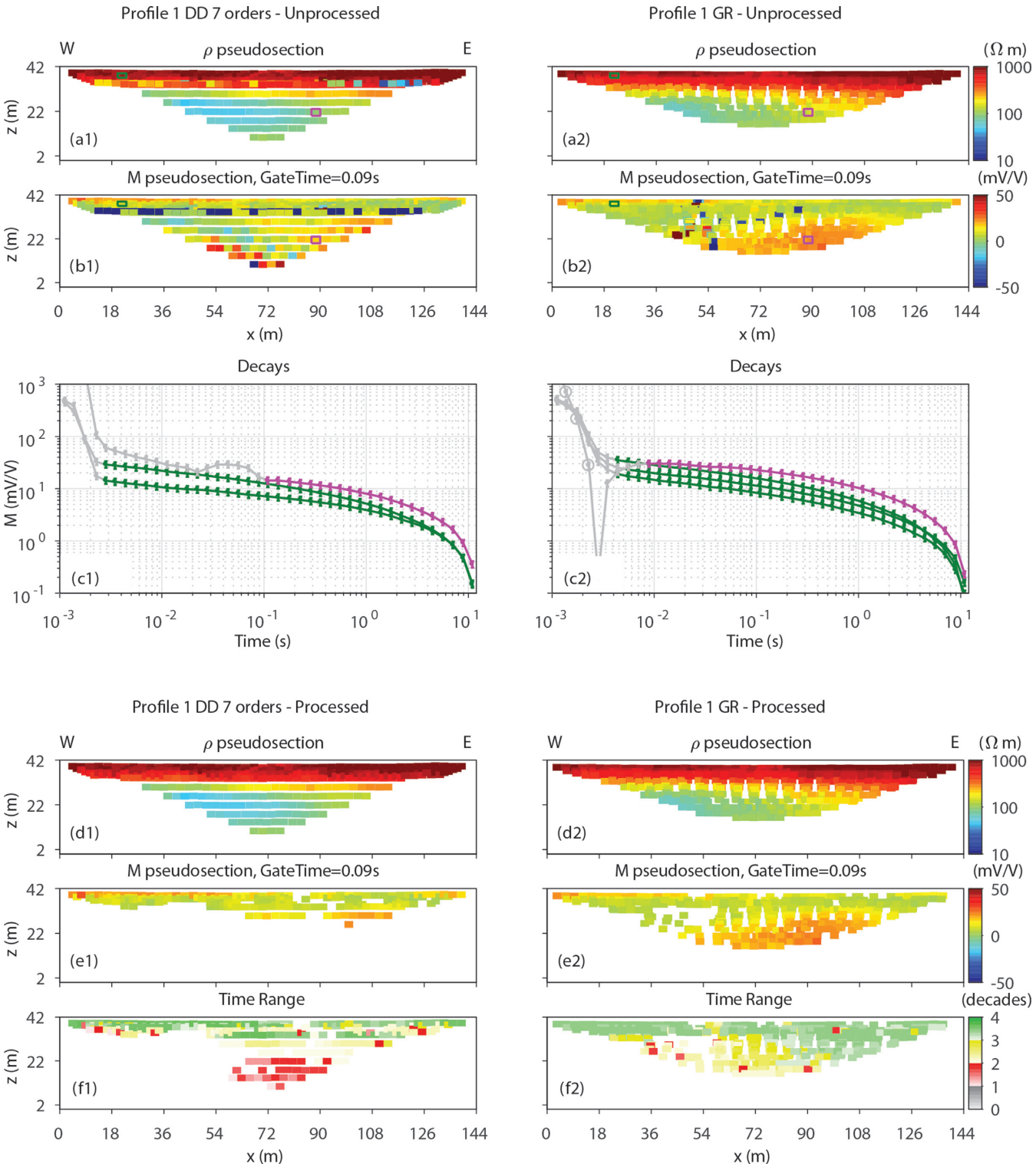

Figure 5. TDIP data of profile 1. Dipole–dipole data are shown on the left and gradient on the right. (a1 and b1) Dipole–dipole unprocessed apparent resistivity and chargeability pseudo-sections. (a2 and b2) Gradient unprocessed apparent resistivity and chargeability pseudo-sections. (c1 and c2) IP decays from the pseudo-section areas highlighted by the magenta and green rectangles, with culled IP data shown in grey colour. (d1 and e1) Dipole–dipole resistivity and chargeability pseudo-sections, after data processing. (d2 and e2) Gradient resistivity and chargeability pseudo-sections, after data processing. (f1 and f2) Time range, in terms of number of decades, for dipole–dipole and gradient data after processing.

Table 4. Processing acceptance rate for sequences described in Table 2.

			After-processing no. data			
			TDIP		FDIP	
		Total number of quadrupoles	No. app. res.	No. decays	No. ampl. spectra	No. phase spectra
Profile 1	GR	693	693 (100 per cent)	489 (71 per cent)	0	0
	DD 7 orders	433	390 (90 per cent)	246 (57 per cent)	372 (86 per cent)	184 (42 per cent)
	DD all orders, A	1377	NA	NA	821 (60 per cent)	330 (24 per cent)
Profile 2	GR and DD 7 orders	1126	1125 (100 per cent)	758 (67 per cent)	NA	NA
	DD all orders, B	2382	NA	NA	1818 (76 per cent)	733 (31 per cent)
Profile 3	GR and DD 7 orders	1126	1126 (100 per cent)	976 (87 per cent)	NA	NA
	DD all orders, C	1081	NA	NA	849 (79 per cent)	393 (36 per cent)

Table 5. Inversion settings.

Model discretization	No. layers	20
	First depth	0.6 m
	Last depth	40 m
Starting model	ρ	Average ρ_a/amplitude
	$\varphi_{\max}$	2 mrad
	τ_φ	0.1 s
	C	0.5
Constraint factors for ρ, $\varphi_{\max}$ and C	Vertical	2.0
	Horizontal	1.15
Constraint factors for τ_φ	Vertical	4.0
	Horizontal	1.45
Data STD factors	ρ_a/amplitude	1.02
	Decays/phase	1.15
Absolute STD	Decays/phase	0.1 mV V^{-1}/0.1 mrad

Fig. 5 shows the TDIP data from profile 1 acquired at Grindsted. Apparent resistivity and chargeability pseudo-sections are plotted before data processing (panels a1 and b1 for DD, and panels a2 and b2 for GR) and after processing (panels d1 and e1 for DD and panels d2 and e2 for GR). The chargeability values are shown at gate 20 ($\sim$ 90 ms) and a few representative IP decays from two different pseudo-depths (magenta and green rectangles in the pseudo-sections) are shown in panel (c1) for DD array and in panel (c2) for GR. Disabled IP gates are grey. The after-processing spectral time ranges of the IP decays, in terms of number of decades, are shown in panels (f1) (DD array) and (f2) (GR array).

Fig. 6 shows the FD data from profile 1 with identical quadrupoles as in the TD dipole–dipole data set of Fig. 5 for comparison purposes (sequence 'DD 7 orders', as described in Table 2); the gradient data are not shown because no usable phase spectra were collected in FD due to the inductive coupling between current and potential cables in nested arrays (Fiandaca 2018 and fig. 11 therein).

Before-processing amplitude and phase pseudo-sections are plotted in panels (a1) and (a2), while after-processing pseudo-sections are shown in panels (c1) and (c2). Amplitude and phase values are shown at 1.25 Hz and a few representative spectra from two different pseudo-depths (magenta and green rectangles in the pseudo-sections) are shown in panels (b1) (amplitude) and (b2) (phase). Culled data points are shown in grey. The after-processing spectral frequency ranges are shown in panels (d1) (amplitude) and (d2) (phase).

Overall, in Figs 5 and 6 the data quality of TD and FD data is influenced by the (voltage) signal level, as shown for TD data in Gazoty *et al.* (2013): the IP signal-to-noise ratio decreases with the geometrical factor and increases with the apparent resistivity/amplitude and chargeability/phase. In this respect, the conductive and non-chargeable area in the western part of the profile, below 10/15 m in depth, is the noisier one. Furthermore, for the TD method the gradient data have significantly better data quality, thanks to the smaller geometrical factor values of the gradient array (see Table 2).

The comparison of single-spread and dual-spread TD data (not shown here for brevity) reveals similar data quality and decays, with small differences sometimes present at early times (typically a few ms at shallow pseudo-depths and up to a few tens of ms at depth), indicating the presence of cross-cable coupling effects. An abrupt change of slope in the decays is often present at early times, indicative of inductive coupling (Fig. 1). These time gates are hence removed in the processing, together with gates presenting non-decaying features (see Figs 5c1 and c2).

The FD phase spectra present a significant change of slope (usually a steep increase) around 1–10 Hz (Fig. 6b2). Furthermore, the FD slope change increases in magnitude and happens at even smaller frequencies in the deeper part of the pseudo-sections.

This phase increase could in theory be due to both EM coupling and/or the spectral characteristics of the investigated media (i.e. due to geology). In the Appendix, a detailed analysis of the spectral characteristics of the acquired data, in comparison to the EM induction coupling, is carried out. We conclude that an explanation of the phase spectra in terms of only geology is not compatible with the data, and that the high-frequency FD data are affected by EM coupling. For this reason, considering that the EM coupling is not modelled in the forward response, the FD data (interpreted as) affected by EM coupling are culled out in the processing. The coupling in the FD data significantly reduces the spectral range of

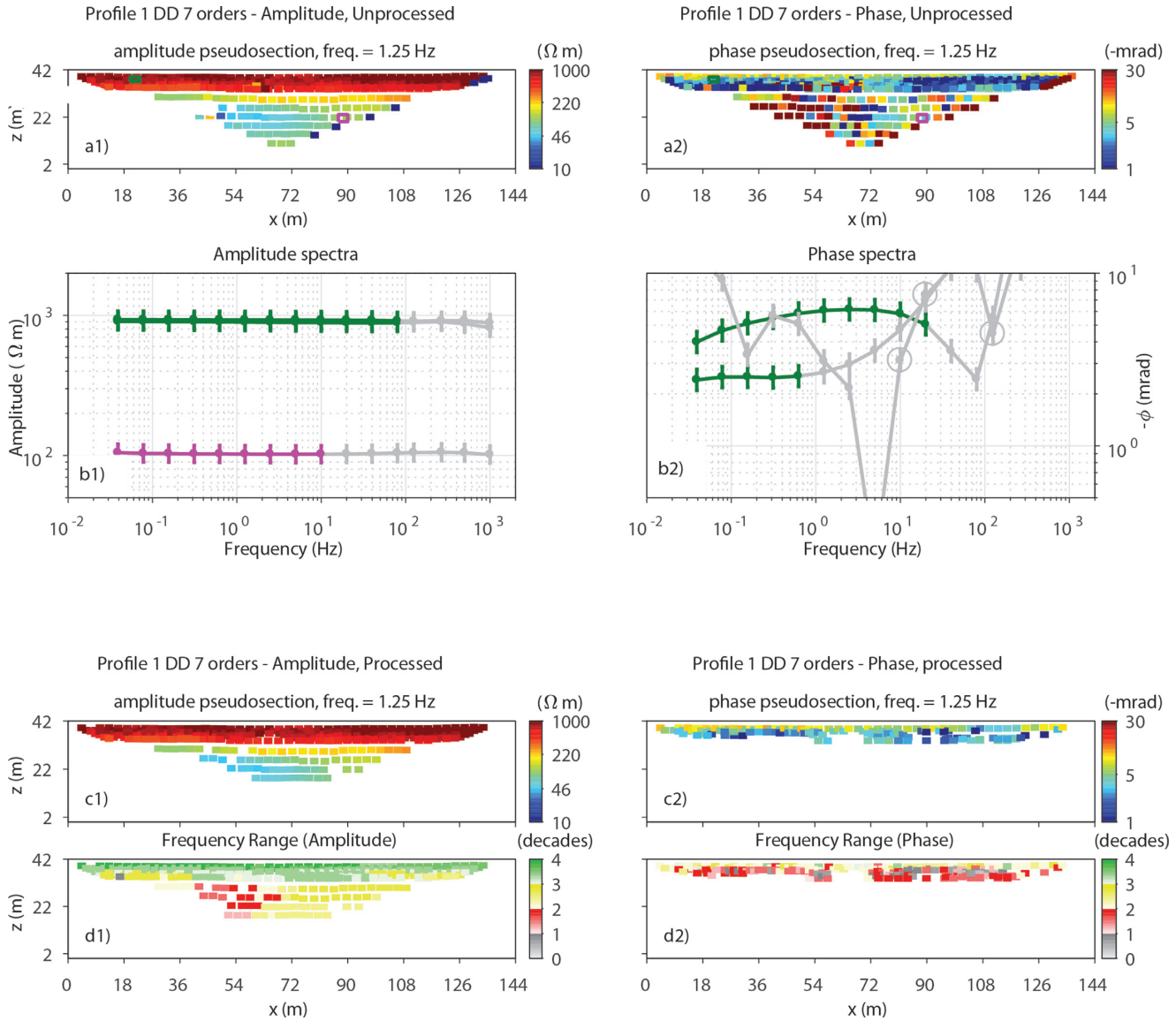

Figure 6. FDIP data of profile 1. Amplitude data are shown on the left and phase on the right, both at 1.25 Hz. (a1 and a2) Amplitude and phase pseudo-sections, before processing. (b1 and b2) Amplitude and phase spectra from the pseudo-section areas highlighted by the magenta and green rectangles, with culled data points shown in grey colour. (c1 and c2) Amplitude and phase pseudo-sections after processing. (b3 and b4) frequency range, in terms of number of decades, for amplitude and phase data after processing.

the phase data, especially at depth (Fig. 6, c2). The effect is much less severe on the amplitude data (Fig. 6c1) and in the TD decays (Figs 5f1 and f2). The after-processing spectral range of the phase data is even smaller than the theoretical induction-free acquisition range (Fiandaca 2018 and fig. 13 therein). This is due to the presence of random noise but possibly also of capacitive coupling (see the Appendix for details). In any case, compared to the TD data, smaller current values were injected (on average 100 mA, compared to the average 500 value of TD data), because of the smaller maximum power of the FD instrument (50 W against 250 W), resulting in lower signal-to-noise ratio in the FD data.

Fig. 7 presents the cumulative histograms of the first usable time gate (a), the total time range (b), the last usable phase frequency (c) and the total frequency range (d), for all the measurements of all profiles. Overall, 80 per cent of the TD decays have more than 3 decades of usable time range with a peak at 3.8 decades. For the FD phase spectra, on average 2 decades are usable after processing, with a peak at 1.8 decades. Finally, Table 4 presents the number of apparent resistivity values and decays kept after processing for all the TD inversion sequences presented in this study, as well as the number of amplitude and phase spectra kept for FD data. On average, 27 per cent of the TD decays where culled in the processing, compared to 70 per cent of the FD phase spectra. The large fraction of the FD measurements that is culled can be explained largely by the different measurement schemes, which leads to the automatic measurement of configurations with large geometric factors, and thus correspondingly small signal-to-noise ratios.

COMPARISON OF INVERSION RESULTS

In order to minimize inversion-related differences in the FD and TD results, all inversions have been carried out within the same inversion framework and with identical inversion settings. The same model discretization (number of layers and layer thicknesses),

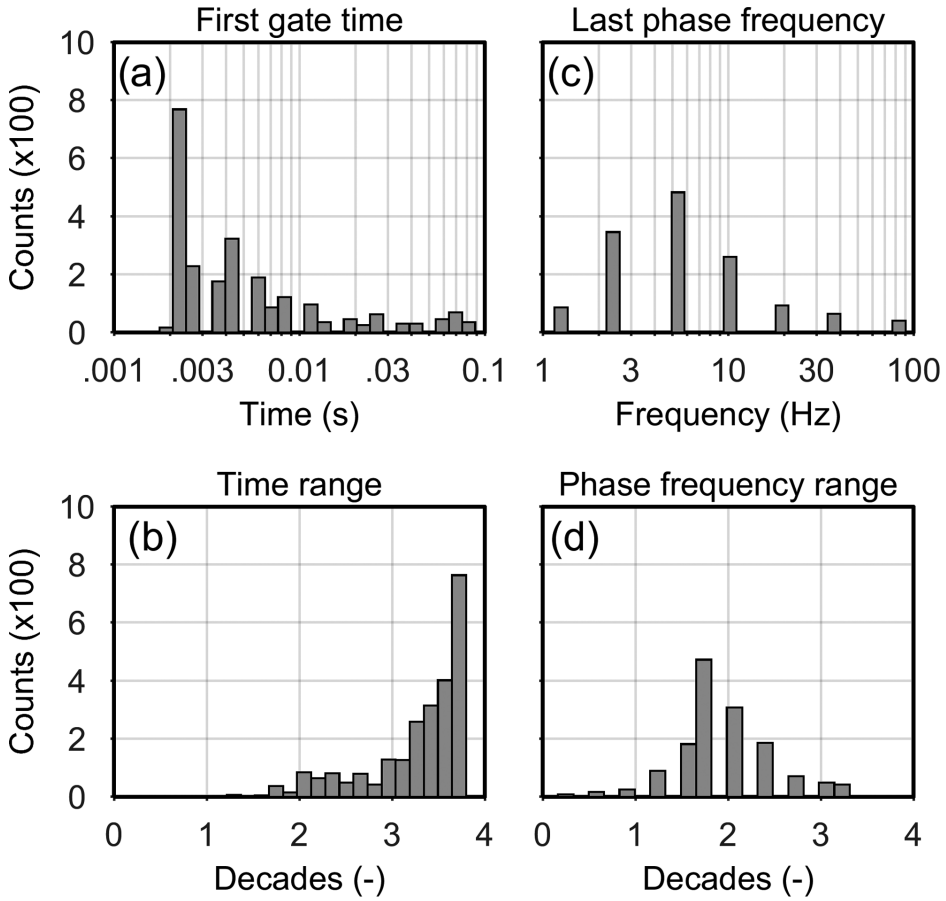

Figure 7. Cumulative histograms of acquisition range for TD/FD measurements of all profiles. (a) First usable time gate. (b) Total time range. (c) Last usable phase frequency. (d) Total frequency range.

model constraints and starting model were used for all TD and FD inversions, as well as the same stopping criteria for the iterative inversion. Furthermore, a similar model for the TD/FD data standard deviations (STDs) has been adopted, which is 2 per cent on apparent resistivity/amplitude and 15 per cent on chargeability/phase shift. In addition, an absolute STD has been added to the relative STD on chargeability/phase data, with value equal to 0.1 mV V^{-1} and 0.1 mrad, respectively. This STD model was found heuristically, searching for an STD model for which it was possible to fit the field data with a final χ misfit close to 1 for both FD and TD data. The inversion settings are summarized in Table 5. The vertical/horizontal constraint values (as well as the data STD) in Table 5 are expressed in terms of STD factors (STDFs). The STDF values represent the relative vertical/lateral variation of the parameters that weights the roughness misfit in the objective function Q of eq. (6) through the covariance matrix $\boldsymbol{C}_R$ of eq. (8). For instance, a vertical constraint value of 2.0 allows roughly 100 per cent vertical variation between the constrained parameters. The same vertical/lateral constraints have been imposed on all parameters except τ_φ for which weaker constraints have been adopted. This choice has been made for avoiding an oversmoothing in the sections of the less-resolved τ_φ parameter.

These settings do not necessarily represent the best possible choice for an individual inversion, but overall the inversion results are satisfactory and the comparison is simple. With a similar reasoning, the ranges of the parameter colour scales are also identical in all the inversion figures.

Inversion of synthetic data

TD and FD inversions were performed on a synthetic MPA Cole–Cole model that mimics the typical geological settings of the Grindsted area, as shown in Figs 8(a1)–(d1). The 1000 Ωm layer in the top 6–7 m represents the quaternary sand layer. The low-resistive (30 Ωm) layer from 6 to 26 m represents the leachate plume from the landfill, underlain by a non-contaminated tertiary sand layer (200 Ωm). Two thin layers approximately 3 m thick, located at the top/bottom boundaries of the leachate plume, represent clay-lignite layers, which are more chargeable ($\varphi_{\max} = 35$ mrad) than the background sand formation ($\varphi_{\max} = 2$ mrad). The parameters τ_φ and C are set to 0.1 s and 0.5 in the background sand and to 1.0 s and 0.3 within the lignite layers, respectively. Synthetic data were calculated using the TD dipole–dipole sequence also employed in the field ('DD 7 orders' in Table 2). For TDIP synthetic data we used 29 time windows, totalling 30 data points (29 IP + 1 resistivity) per quadrupole and, for FDIP, 16 frequencies were used totalling 32 data points (16 amplitudes + 16 phases) per quadrupole. In this way a similar size of data space was simulated for both domains.

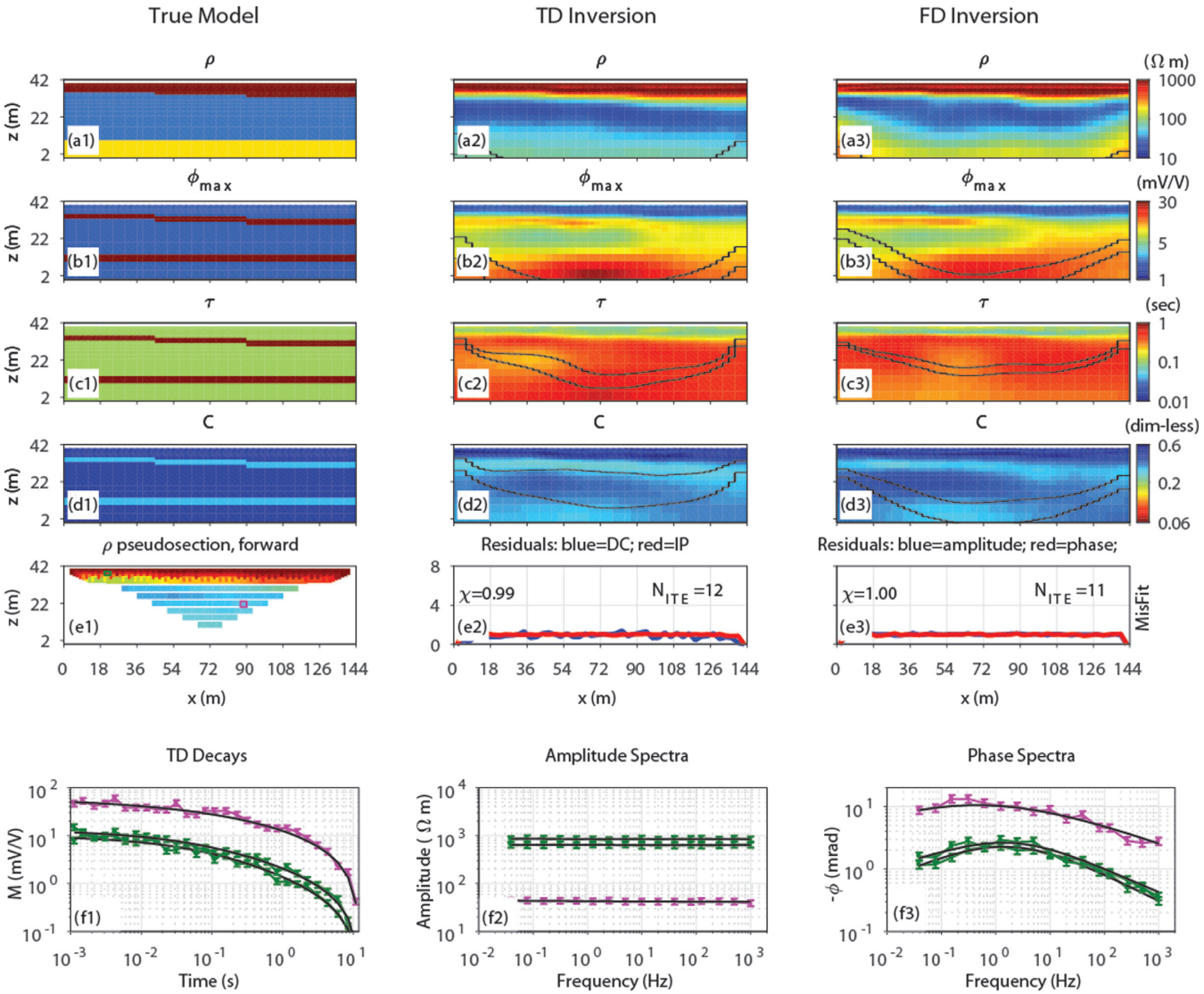

Figure 8. Comparison of FD and TD inversions of synthetic data. (a1–d1) Synthetic MPA Cole-Cole model. (e1) TD apparent resistivity pseudo-section. (a2–d2) TD inversion model. (e2) misfit of DC (blue) and IP (red) data of the TD inversion averaged vertically (and over all gates for the IP misfit) along the pseudo-section. N_{ITE} is the number of iterations. (a3–d3) FD inversion model. (e3) Misfit of amplitude (blue) and phase (red) of the FD inversion averaged vertically and over all frequencies along the pseudo-section. (f1) Synthetic TDIP decays (magenta and green colour) and inversion responses (black curves). (f2) Synthetic FDIP amplitude spectra (magenta and green colour) and inversion responses (black curves). (f3) Synthetic FDIP phase spectra (magenta and green colour) and inversion responses (black curves). The positions of decays/spectra in panels (f1)–(f3) are shown by green and blue square boxes in (e1).

Gaussian noise of 2 per cent on the resistivity/amplitude and 15 per cent plus 0.1 mV V^{-1}/0.1 mrad on the chargeability/phase was added to the data.

The inversion results are shown in Fig. 8, in panels (a2)–(d2) for TD and panels (a3)–(d3) for FD. The DOI is shown for each parameter section by black lines, with an upper (more conservative) and lower (less conservative) estimation. Both inversions fit the data with $\chi = 1$ (panels e1 and e2) and all the inversion sections are qualitatively and quantitatively very similar for all parameters. While the inverted resistivity sections resemble the true model resistivity correctly, the two thin chargeable layers are not resolved equally well. In both inversions parameter contrasts smaller than the true ones are retrieved, the shallower chargeable layer is not clearly delineated in the right side of the model and the thickness of the deeper chargeable layer is greatly overestimated. The layering in C parameter is decently imaged, while the τ_φ values are highly overestimated in the non-chargeable area comprised between the chargeable layers. However, the structures in the φ_{max}, τ_φ and C sections are very similar in FD and TD, and, to a minor extent, the DOI estimates. In the synthetic simulations the entire acquisition TD and FD ranges were simulated (Table 1), without considering any range decrease due to noise/coupling issues. This enables assessment of the ability to retrieve the IP parameters with equivalent ranges of acquisition.

Inversion of field data

Fig. 9 displays a detailed, one-to-one comparison of the TD and FD inversions of profile 1. Two sets of inversion results are compared: (1) inversions with identical quadrupolar sequence (panels a1–e1 for TD and panels a2–e2 for FD); (2) inversions of all the collected data points (panels a3–e3 for TD and panels a4–e4 for FD). The identical quadrupolar sequence is a subset of the 'DD 7 orders' sequence of Table 2, obtained by taking the intersection of enabled data points in resistivity/amplitude (340 quadrupoles) and decay/phase (145 quadrupoles) of the TD and FD processed data. This is done in order to minimize discrepancies in the inversion models due to different sizes of data spaces. In the inversions of all the collected data points, the TD sequence is composed by the processed dipole–dipole and gradient sequences merged together ('GR' and 'DD 7 orders' sequences, Table 2), while the FD sequence is composed by processed dipole–dipole data without limitations on the maximum measured order ('DD all orders A', Table 2). The inversion results of the two El-logs B1 and B2 are superimposed on the top of all Cole-Cole MPA parameters.

The FD and TD inversion results obtained inverting identical data sequences agree very well for all parameters. In the resistivity sections (a1 and a2) the top quaternary sand layer (first 10–12 m) is highly resistive (>500 Ωm), while the landfill leachate plume is observed as a low-resistive anomaly in the tertiary sand formation (<30 Ωm). Overall, the resistivity distribution retrieved by the inversion of surface data correlates well with both El-log resistivity models, with an overestimation of the resistivity values in the deep low-resistive plume seen in B2 (between 15 and 26 m depth).

In the φ_{max} sections (b1 and b2), the quaternary sand has low phase values (∼2–3 mrad). The signature of the top lignite layer can be seen as a high-chargeability anomaly around 10 m depth; the τ_φ sections show the same order of magnitude as compared to El-log inversions in both domains, while the C sections show values slightly higher than the El-log ones at depth. Overall, the DOI is limited in φ_{max} and C and very shallow in τ_φ. This is explained by the amount of data culled out during processing, because of the coupling present in the phase spectra and the general low signal-to-noise ratio of the data, due to the high conductivity of the leachate plume and the high values of the dipole–dipole geometrical factor (Gazoty *et al.* 2013).

However, when including the gradient data in the TD inversion we observe a significant improvement in the depth of investigation, for all parameters (panels a3–d3). Unfortunately, similarly to what happens in the synthetic example on the right side of the model, the vertical resolution of the surface inversion is not enough to resolve the layering observed in the El-log inversions. In particular, the low φ_{max} anomaly seen in the B2 El-log inversion between 17 and 26 m in depth is not resolved in the surface inversion. Furthermore, while the El-log inversions show at depth a few thin layers with increased τ_φ values, the τ_φ section presents a general increase with depth without significant vertical variability. Again, this is a lack of vertical resolution similar to what it is shown in the synthetic example.

Also, the inversion of the full FD data set, including more dipole-dipole orders (panels a4–d4), improves the inversion results, but within a limited DOI. Again, this is due to fact that the high-order dipole–dipole data were affected by coupling/noisy and many data were culled during processing. Nevertheless, above the DOI a good agreement between the TD and FD spectral parameters is observed.

This can be evidenced by calculating the FD forward data using the TD model inversion (and vice versa), as shown in Fig. 10 for a few representative quadrupoles (the positions of the data points on the pseudo-sections are the same shown in Figs 5 and 6). Both the FD and TD forward responses match the observed data well.

Overall, we conclude that for the identical data sets the TD and FD methods give equivalent inversion results for all IP parameters, but more information at depth is gained from the TD inversion when the gradient sequence is taken into account.

Fig. 11 shows the inversion results of profiles 2 and 3, collected at Pillemark. In profile 2, a conductive and chargeable anomaly (panels a1 and a2, and b1 and b2) clearly delineates the landfill waste in both FD and TD inversions, with similar lateral extent (0–72 m along the profile) and thickness (approximately 6–8 m). Once again, the τ_φ and C sections show similar patterns and DOI.

Profile 3 was collected outside the landfill area without leachate or waste. The lithological information available from a nearby borehole (Fig. 2) is superimposed on the inversion. A good correlation is observed between the geology and inverted resistivity sections (a3 and a4) and φ_{max} sections (b3 and b4). The top lithological unit (approx. 3.1 m thick) consists of silt/silty sand and shows moderate to high resistivity values (up to ∼200 Ωm) and φ_{max} values (∼10 mrad). Below the silt layer a thin (0.9 m) non-resolved clay layer is present, followed by a sand layer (4.3 m thick) characterized by low phase values (∼2–3 mrad) in both inversions. Finally, the clay-till layer (16 m thick) located below the sand is characterized by low resistivity and moderate φ_{max} values.

DISCUSSION

The results of this study are encouraging: the theoretical equivalence of the TD and FD spectral imaging has been verified on real field measurements, with similar results in terms of retrieved spectral information, especially when identical quadrupolar sequences are inverted. Nevertheless, significant differences between the measurements in the different domains have been highlighted, mainly in terms of sequence selection, acquisition range and acquisition time.

The differences in the after-processing acquisition ranges are due to the difficulty of distinguishing inductive and capacitive coupling from the IP effect. The coupling issue depends considerably on the cable layout and the capacitive coupling is system-specific, but it is more severe in the FD because the current is continuously flowing in the current cables during acquisition with a resulting continuous EM interference with the potential measurements.

While the capacitive coupling can be diminished, for instance decreasing the contact resistance at electrodes, the inductive coupling is unavoidable. Instead of the simple culling of coupled data, other approaches have been proposed in the literature for handling the coupling. Typically, the measured spectra are fitted with a double-relaxation model (e.g. double Cole-Cole) and the high-frequency relaxation representing the coupling is removed from the data before interpretation (Pelton *et al.* 1978a). The limitation of this approach is that it does not take the physics behind the coupling effect into account, and nothing ensures that only the coupling is removed in the processing, as shown for instance by Ingeman-Nielsen & Baumgartner (2006); Ingeman-Nielsen & Baumgartner (2006) after showing the poor performance of the coupling removal with a double-relaxation model advocate the use of physics-based approaches based on actual EM equations and resistivity structure for dealing with the inductive coupling. This is done for instance by Kang & Oldenburg (2017) with a 3-D EM removal.

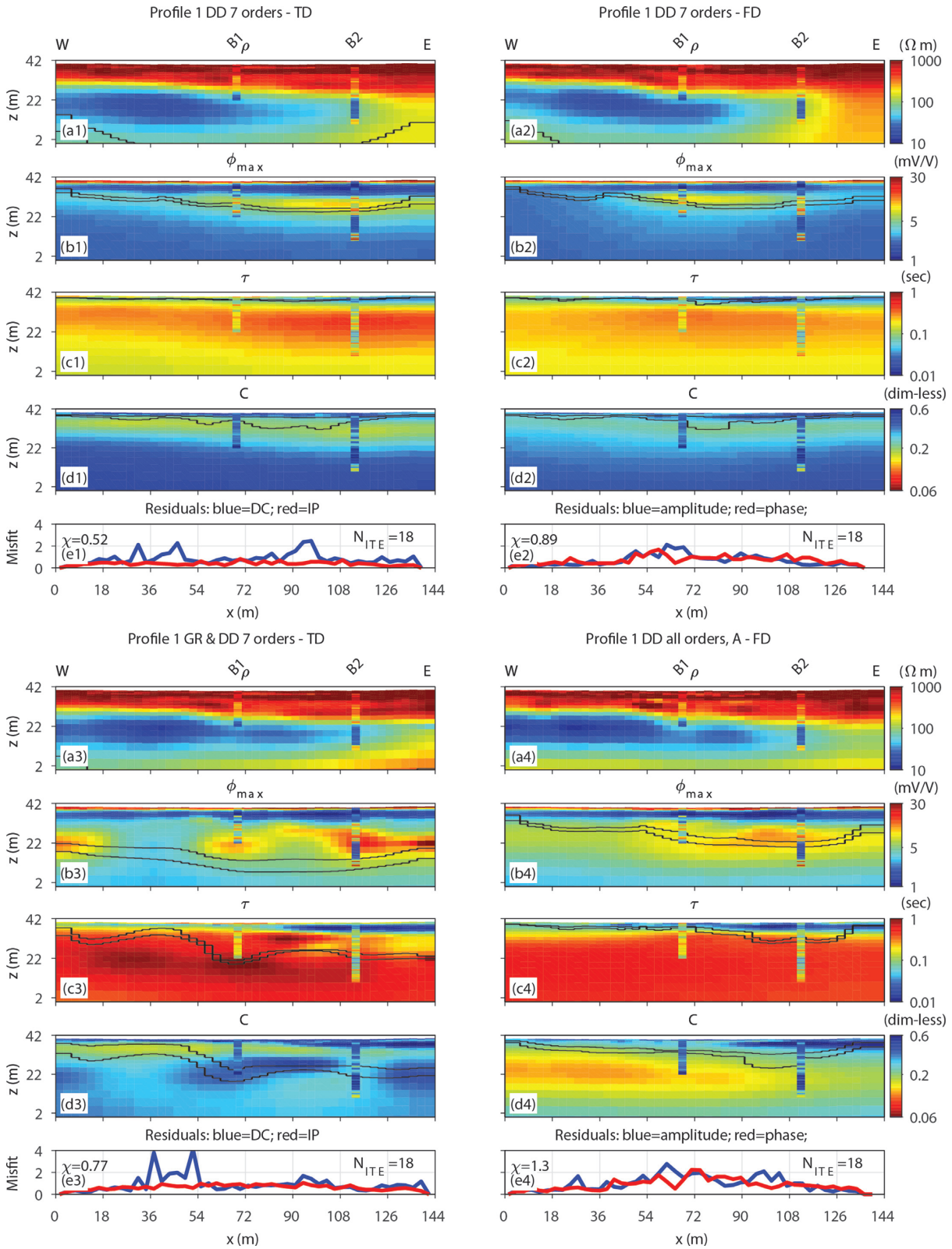

Figure 9. TD (left) and FD (right) inversion results of profile 1. (a1–e1) TD inversion results with sequence 'DD 7 orders' from Table 2. (a2–e2) FD inversions results with sequence 'DD 7 orders' from Table 2. (a3–e3) TD inversion results with sequence 'GR' and 'DD 7 orders' from Table 2. (a4–e4) FD inversion results with sequence 'DD all orders A' from Table 2.

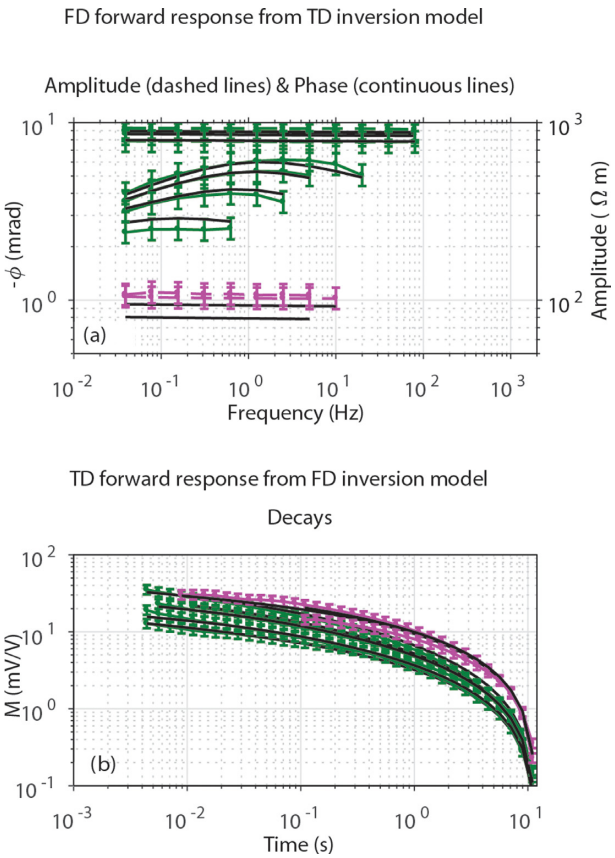

Figure 10. (a) Comparison of FD forward responses computed using the TD inversion model versus FD field data of profile 1. (b) Comparison of TD forward responses computed using the FD inversion model versus TD field data of profile 1. Forward responses are shown in black and field data in magenta/green. The locations of the quadrupoles in the pseudo-sections are highlighted by the magenta/green rectangles in Figs 4 and 5.

Recently, methods have been presented for modelling-based removal of both inductive and capacitive coupling, for borehole applications (Zhao *et al.* 2013), cross-hole applications (Zhao *et al.* 2014) and surface measurements (Zimmermann *et al.* 2016; Kang & Oldenburg 2017). All these methods require an accurate knowledge of the cable relative positions for the removal of the inductive coupling, and fan-like cable layouts have been proposed for surface applications (Zimmermann *et al.* 2016). This limits the actual usability of the correction in the field considerably, especially when electrode distances bigger than 1 m are used. Hence, low-noise sequences with nested dipoles, like the gradient array, are still very difficult to use in big-scale field FD applications. Furthermore, Zimmermann *et al.* (2016) points out that you actually need a model-dependent correction, which takes the leakage current and the total parasitic capacity between system ground and the soil into account.

On the contrary, in TD a much wider induction-free acquisition time can be measured, also with nested arrays with really close current and potential lines, as in multichannel cables (Fiandaca 2018). The cross-cable capacitively induced signal not only decreases with the cable separation, but also depends on the contact resistance at the electrodes (Dahlin & Leroux 2012). When the contact resistances are in the kΩ range and multichannel cables are used, the coupling is often significant at early times in TD acquisitions. However, watering the electrodes and/or using dual-spread cable layout (Dahlin & Leroux 2012) is most often enough to reduce the coupling, and the actual modelling of the cross-cable capacitance is not needed as well.

Regarding the data acquisition time, the tenfold difference between the FD and TD approaches evidenced in this study is system-specific because only a twofold difference is expected from a theoretical point of view with the used settings. The new version of the FD instrument used in this study, that is, the SIP256D (Radic 2016), has been recently released and performs a Fourier transform of the signal at the units for improving the transfer time. This should decrease the difference between theoretical and actual measurement times.

Finally, the inversion approach followed in this study uses a parametrization of the IP phenomenon, which forces the shape of the conductivity/phase spectra. This approach has proven to be applicable with the presented data, which can be modelled with a single-peak relaxation model (when the high-frequency FD data, affected by EM coupling, are culled out) and has the advantage of structurally imposing the smoothness of the conductivity/phase spectra. Nevertheless, more flexible inversion approaches, for instance in terms of Debye decomposition, can be used both in FD (Nordsiek & Weller 2008) and TD (Tarasov & Titov 2007). However, more complex approaches have to be required by the data, and complex spectra need wide acquisition ranges to be resolved (for instance, five decades in Tarasov & Titov 2007). With the single-peak MPA model used in this study and similar acquisition settings, Fiandaca (2018) shows that a wider acquisition range means increased spectral content and parameter resolution, for both FD and TD data, and that the TD approach has a better resolution of the spectral parameters then the FD approach, when the induction-free acquisition range is used. These results are valid also in this field comparison, considering that the difference in acquisition range on the presented field data is even bigger than the difference in theoretical induction-free acquisition range.

CONCLUSIONS

We have presented a comparison study of the TD and FD spectral IP methods in terms of acquisition time, data quality and spectral information retrieved from inversion. We collected TD and FD surface measurements on three profiles with different lithology. In addition, TDIP data were collected in two boreholes using a drilling technique in which apparent formation resistivity and chargeability values are measured during drilling.

The comparisons reveal that TD and FD results are comparable not only qualitatively, but also quantitatively. Furthermore, the surface inversions are in agreement with the borehole results and lithology.

However, we document differences for the acquisition range and acquisition time of the two methods. The recent advancements in signal processing of full-waveform TD data with harmonic denoising and advanced background removal have increased the measurable TD acquisition range up to almost four decades in time, starting from 2–3 ms after the current switch. With the FD instrument used in this study the acquisition range was much smaller, which we attribute to cross-cable coupling when measuring above 1–10 Hz. Furthermore, the FD cross-cable induction prevents the measurement of nested arrays, limiting the choice of the measurement sequences. Regarding the acquisition time, the TD acquisition was approximately 10 times faster than the FD acquisition with

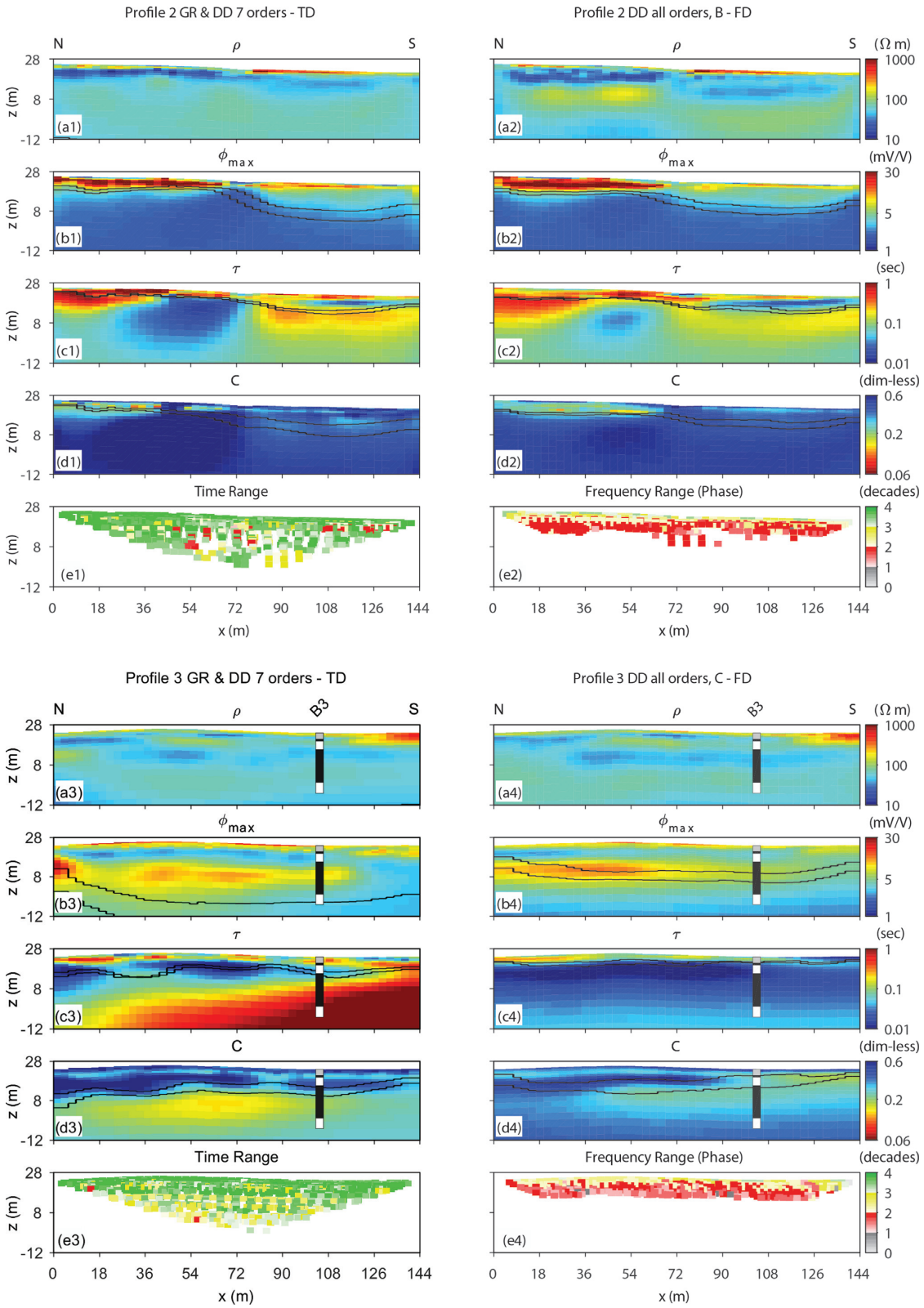

Figure 11. TD (left) and FD (right) inversion results of profile 2 (top) and profile 3 (bottom). (a1–e1) TD inversion results and time range of profile 2, with sequence 'GR' and 'DD 7 orders' from Table 2. (a2–e2) FD inversion results and frequency range of profile 2, with sequence 'DD all orders B' from Table 2. (a3–e3) TD inversion results and time range of profile 3, with sequence 'GR' and 'DD 7 orders' from Table 2. (a4–e4) FD inversion results and frequency range of profile 3, with sequence 'DD all orders C' from Table 2. Legend of lithological logs: grey—silt/sand; white—sand; black—clay/till.

analogous spectral range. This result is mainly due to the FD instrument used in the comparison because the sum of the periods of all the acquired frequencies is only two times the TD acquisition time.

The results confirm the comparability of the FD and TDIP methods and pave the way for a more extended use of IP in the field for a quantitative estimation of the spectral parameters and for comparing field, laboratory and theoretical results.

ACKNOWLEDGEMENTS

The financial support for this work was provided by the research project GEOCON, advancing geological, geophysical and contaminant monitoring technologies for contaminated site investigation (contract 1305-00004B). The funding for GEOCON is provided by the Danish Council for Strategic Research under the Programme Commission on Sustainable Energy and Environment. Authors would also like to thank to Myriam Lajaunie, Johannes Kenkel, Andreas Kemna and Maximilian Weigand for their contributions in the field data collection.

REFERENCES

Attwa, M. & Günther, T., 2013. Spectral induced polarization measurements for predicting the hydraulic conductivity in sandy aquifers, *Hydrol. Earth Syst. Sci.,* **17,** 4079–4094.

Auken, E. *et al.*, 2015. An overview of a highly versatile forward and stable inverse algorithm for airborne, ground-based and borehole electromagnetic and electric data, *Explor. Geophys.,* **2015,** 223–235.

Chongo, M., Christiansen, A.V., Fiandaca, G., Nyambe, I.A., Larsen, F. & Bauer-Gottwein, P., 2015. Mapping localised freshwater anomalies in the brackish paleo-lake sediments of the Machile–Zambezi Basin with transient electromagnetic sounding, geoelectrical imaging and induced polarisation, *J. Appl. Geophys.,* **123,** 81–92.

Dahlin, T. & Leroux, V., 2012. Improvement in time-domain induced polarization data quality with multi-electrode systems by separating current and potential cables, *Near Surf. Geophys.,* **10,** 545–565.

Dey, A. & Morrison, H.F., 1973. Electromagnetic coupling in frequency and time-domain induced polarization surveys over a multilayered Earth, *Geophysics,* **38,** 380–405.

Doetsch, J., Fiandaca, G., Auken, E., Christiansen, A.V., Cahill, A.G. & Jacobsen, J.D., 2015a. Field scale time-domain spectral induced polarization monitoring of geochemical changes induced by injected CO_2 in a shallow aquifer, *Geophysics,* **80,** WA113–WA126.

Doetsch, J., Ingemann-Nielsen, T., Christiansen, A.V., Fiandaca, G., Auken, E. & Elberling, B., 2015b. Direct current (DC) resistivity and induced polarization (IP) monitoring of active layer dynamics at high temporal resolution, *Cold Reg. Sci. Technol.,* **119,** 16–28.

Fiandaca, G., 2018. Induction-free acquisition range in spectral time- and frequency-domain induced polarization at field scale, *Geophys. J. Int.*

Fiandaca, G., Auken, E., Gazoty, A. & Christiansen, A.V., 2012. Time-domain induced polarization: full-decay forward modeling and 1D laterally constrained inversion of Cole-Cole parameters, *Geophysics,* **77,** E213–E225.

Fiandaca, G., Ramm, J., Binley, A., Gazoty, A., Christiansen, A.V. & Auken, E., 2013. Resolving spectral information from time domain induced polarization data through 2-D inversion, *Geophys. J. Int.,* **192,** 631–646.

Fiandaca, G., Christiansen, A.V. & Auken, E., 2015a. Depth of investigation for multi-parameters inversions, in *21st European Meeting of Environmental and Engineering Geophysics,* Turin, Italy.

Fiandaca, G., Doetsch, J., Vignoli, G. & Auken, E., 2015b. Generalized focusing of time-lapse changes with applications to direct current and time-domain induced polarization inversions, *Geophys. J. Int.,* **203,** 1101–1112.

Fiandaca, G., Maurya, P.K. & Madsen, L.M., 2017. Re-parameterization of the Cole-Cole model for improved spectral inversion of induced polarization data, in *23rd European Meeting of Environmental and Engineering Geophysics,* Near Surface Geoscience, Malmo, Sweden.

Fiandaca, G., Madsen, L.M. & Maurya, P.K., 2018. Re-parameterizations of the Cole-Cole model for improved spectral inversion of induced polarization data, in press Near Surface Geophysics, .

Flores Orozco, A., Kemna, A., Oberdörster, C., Zschornack, L., Leven, C., Dietrich, P. & Weiss, H., 2012. Delineation of subsurface hydrocarbon contamination at a former hydrogenation plant using spectral induced polarization imaging, *J. Contaminant Hydrol.,* **136–137,** 131–144.

Gazoty, A., Fiandaca, G., Pedersen, J., Auken, E. & Christiansen, A.V., 2012a. Mapping of landfills using time-domain spectral induced polarization data: the Eskelund case study, *Near Surf. Geophys.,* **10,** 575–586.

Gazoty, A., Fiandaca, G., Pedersen, J., Auken, E., Christiansen, A.V. & Pedersen, J.K., 2012b. Application of time domain induced polarization to the mapping of lithotypes in a landfill site, *Hydrol. Earth Syst. Sci.,* **16,** 1793–1804.

Gazoty, A., Fiandaca, G., Pedersen, J., Auken, E. & Christiansen, A.V., 2013. Data repeatability and acquisition techniques for Time-Domain spectral Induced Polarization, *Near Surf. Geophys.,* **11,** 391–406.

Günther, T. & Martin, T., 2016. Spectral two-dimensional inversion of frequency-domain induced polarization data from a mining slag heap, *J. appl. Geophys.,* **2016,** 10.

Hönig, M. & Tezkan, B., 2007. 1D and 2D Cole-Cole-inversion of time-domain induced-polarization data, *Geophys. Prospect.,* **55,** 117–133.

Hördt, A., Hanstein, T., Hönig, M. & Neubauer, F.M., 2006. Efficient spectral IP-modelling in the time domain, *J. Appl. Geophys.,* **59,** 152–161.

Hördt, A., Druiventak, A., Blaschek, R., Binot, F., Kemna, A., Kreye, P. & Zisser, N., 2009. Case histories of hydraulic conductivity estimation with induced polarization at the field scale, *Near Surf. Geophys.,* **7,** 529–545.

Ingeman-Nielsen, T., 2006. The effect of electrode contact resistance and capacitive coupling on complex resistivity measurements, in *SEG Technical Program Expanded Abstracts 2006,* pp. 1376–1380, Society of Exploration Geophysicists.

Ingeman-Nielsen, T. & Baumgartner, F., 2006. Numerical modelling of complex resistivity effects on a homogenous half-space at low frequencies, *Geophys. Prospect.,* **54,** 261–271.

Johansen, H.K. & Sørensen, K.I., 1979. Fast Hankel transforms, *Geophys. Prospect.,* **27,** 876–901.

Johansson, S., Fiandaca, G. & Dahlin, T., 2015. Influence of non-aqueous phase liquid configuration on induced polarization parameters: Conceptual models applied to a time-domain field case study, *J. Appl. Geophys.,* **123,** 295–309.

Johansson, S., Sparrenbom, C., Fiandaca, G., Lindskog, A., Olsson, P.-I., Dahlin, T. & Rosqvist, H., 2016. Investigations of a Cretaceous limestone with spectral induced polarization and scanning electron microscopy, *Geophys. J. Int.,* **208,** 954–972.

Johnson, I.M., 1984. Spectral induced polarization parameters as determined through time-domain measurements, *Geophysics,* **49,** 1993–2003.

Kang, S. & Oldenburg, D.W., 2017. TEM-IP: extracting more induced polarisation information from grounded source time domain electromagnetic data, *Geophys. Prospect.,* **66,** 74–86

Kemna, A., Binley, A., Ramirez, A. & Daily, W., 2000. Complex resistivity tomography for environmental applications, *Chem. Eng. J.,* **77,** 11–18.

Kemna, A., Binley, A. & Slater, L., 2004. Crosshole IP imaging for engineering and environmental applications, *Geophysics,* **69,** 97–107.

Kemna, A. *et al.*, 2012. An overview of the spectral induced polarization method for near-surface applications, *Near Surf. Geophys.,* **10,** 453–468.

Kemna, A., Huisman, J.A., Zimmermann, E., Martin, R., Zhao, Y., Treichel, A., Flores Orozco, A. & Fechner, T., 2014. Broadband electrical impedance tomography for subsurface characterization using improved corrections of electromagnetic coupling and spectral regularization, in

Tomography of the Earth's Crust: From Geophysical Sounding to Real-Time Monitoring: Geotechnologien Science Report No. 21, pp. 1–20, eds Weber, M. & Münch, U., Springer International Publishing.

Kenkel, J. & Kemna, A., 2017. Sensitivity of 2-D complex resistivity measurements to subsurface anisotropy, *Geophys. J. Int.,* **208,** 1043–1057.

Kjeldsen, P., Bjerg, P.L., Rugge, K., Christensen, T.H. & Pedersen, J.K., 1998. Characterization of an old municipal landfill (Grindsted, Denmark) as a groundwater pollution source: landfill hydrology and leachate migration, *Waste Manage. Res.,* **16,** 14–22.

Komarov, V.A., 1980. *Electrorazvedka Metodom Vyzvannoi Polarizatsii (Electrical Prospecting Using Induced Polarisation Method),* Nedra (In Russian).

Leroy, P. & Revil, A., 2009. A mechanistic model for the spectral induced polarization of clay materials, *J. geophys. Res.,* **114,** doi:10.1029/2008JB006114.

Loke, M.H., Chambers, J.E. & Ogilvy, R.D., 2006. Inversion of 2D spectral induced polarization imaging data, *Geophys. Prospect.,* **54,** 287–301.

Madsen, L., Fiandaca, G., Christiansen, A. & Auken, E., 2017a. Resolution of well-known resistivity equivalences by inclusion of time-domain induced polarization data, *Geophysics,* **83,** E47–E54.

Madsen, L.M., Fiandaca, G., Auken, E. & Christiansen, A.V., 2017b. Time-domain induced polarization – an analysis of Cole–Cole parameter resolution and correlation using Markov Chain Monte Carlo inversion, *Geophys. J. Int.,* **211,** 1341–1353.

Marshall, D.J. & Madden, T.R., 1959. Induced polarization, a study of its cuases, *Geophysics,* **24,** 790–816.

Maurya, P.K., Rønde, V.K., Fiandaca, G., Balbarini, N., Auken, E., Bjerg, P.L. & Christiansen, A.V., 2017. Detailed landfill leachate plume mapping using 2D and 3D electrical resistivity tomography - with correlation to ionic strength measured in screens, *J. Appl. Geophys.,* **138,** 1–8.

Maurya, P.K., Balbarini, N., Møller, I., Rønde, V., Christiansen, A.V., Bjerg, P.L., Auken, E. & Fiandaca, G., 2018. Subsurface imaging of water electrical conductivity, hydraulic permeability and lithology at contaminated sites by induced polarization, *Geophys. J. Int.,* **213,** 770–785.

Nordsiek, S. & Weller, A., 2008. A new approach to fitting induced-polarization spectra, *Geophysics,* **73,** F235–F245.

Oldenburg, D.W. & Li, Y., 1994. Inversion of induced polarization data, *Geophysics,* **59,** 1327–1341.

Olsson, P.I., Dahlin, T., Fiandaca, G. & Auken, E., 2015. Measuring time-domain spectral induced polarization in the on-time:decreasing acquisition time and increasing signal-to-noise ratio, *J. Appl. Geophys.,* **123,** 316–321.

Olsson, P.-I., Fiandaca, G., Larsen, J.J., Dahlin, T. & Auken, E., 2016. Doubling the spectrum of time-domain induced polarization by harmonic de-noising, drift correction, spike removal, tapered gating and data uncertainty estimation, *Geophys. J. Int.,* **207,** 774–784.

Orozco, A.F., Kemna, A., Oberdörster, C., Zschornack, L., Leven, C., Dietrich, P. & Weiss, H., 2012. Delineation of subsurface hydrocarbon contamination at a former hydrogenation plant using spectral induced polarization imaging, *J. Contaminant Hydrol.,* **136–137,** 131–144.

Orozco, A.F., Williams, K.H. & Kemna, A., 2013. Time-lapse spectral induced polarization imaging of stimulated uranium bioremediation, *Near Surf. Geophys.,* **11,** 531–544.

Pelton, W.H., Rijo, L. & C.M.JR., S., 1978a. Inversion of two-dimensional resistivity and induced-polarization data, *Geophysics,* **43,** 788–803.

Pelton, W.H., Ward, S.H., Hallof, P.G., Sill, W.R. & Nelson, P.H., 1978b. Mineral discrimination and removal of inductive coupling with multifrequency IP, *Geophysics,* **43,** 588–609.

Radic, T., 2016. Concept of our New Multi-Channel SIP Instrument:SIP256D, in *4th International Workshop on IP,* Aarhus, Denmark.

Routh, P., Oldenburg, D. & Li, Y., 1998. Regularized in version of spectral IP parameters from complex resistivity data, in *SEG Technical Program Expanded Abstracts 1998,* pp. 810–813, Society of Exploration Geophysicists.

Sato, H.K., 2000. Potential field from a dc current source arbitrarily located in a nonuniform layered medium, *Geophysics,* **65,** 1726–1732.

Seigel, H., Nabighian, M., Parasnis, D. & Vozoff, K., 2007. The early history of the induced polarization method, *Leading Edge,* **26,** 312–321.

Shuey, R.T. & Johnson, M., 1973. On the phenomenology of electrical relaxation in rocks, *Geophysics,* **38,** 37–48.

Slater, L.D. & Glaser, D.R., 2003. Controls on induced polarization in sandy unconsolidated sediments and application to aquifer characterization, *Geophysics,* **68,** 1547–1558.

Slater, L.D. & Lesmes, D., 2002. IP interpretation in environmental investigations, *Geophysics,* **67,** 77–88.

Sunde, E.D., 1968. *Earth Conduction Effects in Transmission Systems,* Dover Publications Inc.

Tarasov, A. & Titov, K., 2007. Relaxation time distribution from time domain induced polarization measurements, *Geophys. J. Int.,* **170,** 31–43.

Van Voorhis, G.D., Nelson, P.H. & Drake, T.L., 1973. Complex resistivity spectra of porphyry copper mineralization, *Geophysics,* **38,** 49–60.

Wemegah, D.D., Fiandaca, G., Auken, E., Menyeh, A. & Danuor, S.K., 2017. Spectral time-domain induced polarisation and magnetic surveying– an efficient tool for characterisation of solid waste deposits in developing countries, *Near Surf. Geophysics,* **15,** 75–84.

Wong, J., 1979. An electrochemical model of the induced-polarization phenomenon in disseminated sulfide ores, *Geophysics,* **44,** 1245–1265.

Yuval & Oldenburg, D.W., 1997. Computation of Cole-Cole parameters from IP data, *Geophysics,* **62,** 436–448.

Zhao, Y., Zimmermann, E., Huisman, J.A., Treichel, A., Wolters, B., van Waasen, S. & Kemna, A., 2013. Broadband EIT borehole measurements with high phase accuracy using numerical corrections of electromagnetic coupling effects, *Meas. Sci. Technol.,* **24,** 085005, .

Zhao, Y., , , Zimmermann, E., Huisman, J.A., Treichel, A., Wolters, B., van Waasen, S. & Kemna, A., 2014. Phase correction of electromagnetic coupling effects in cross-borehole EIT measurements, *Meas. Sci. Technol.,* **26,** 015801, .

Zimmermann, E., Huisman, J.A., van Mester, A. & Waasen, S., 2016. Numerical correction of phase errors due to leakage currents in wideband EIT measurements, in *4th international Workshop on IP*, Aarhus, Denmark.

Zonge, K. & Hughes, L., 1985. Effect of electrode contact resistance on electric field measurements, in *SEG Technical Program Expanded Abstracts 1985,* pp. 231–234, Society of Exploration Geophysicists.

Zonge, K.L., Sauck, W.A. & Sumner, J.S., 1972. Comparison of time, frequency, and phase measurements in induced polarization, *Geophys. Prospect.,* **20,** 626–648.

APPENDIX

The FD phase spectra, on all profiles, present an increase in phase with increasing frequency, often with a significant change of slope in the frequency range between 1 and 100 Hz. The phase increase happens at earlier frequencies for dipoles with greater order (deeper in the pseudo-section), but the slope of the high-frequency trend is almost constant in a log–log plot: the spectra tend to a linear growth with frequency. The TD decays show a step increase of values in the first few milliseconds after the current switch, certainly due to the finite duration of the current switch (that usually is completed within the first millisecond after the switch) and the resulting EM induction effects. Furthermore, significant changes of slope at the early times are sometimes present in the first one-two decades after the current switch, possibly accompanied by a change of sign.

A high-frequency linear growth of the FD phase with frequency is typical of a polarization mechanism dominated by dielectric processes in which the effective imaginary conductivity $i\ \sigma''_{\text{eff}} = \text{i}\sigma''\ + \text{i}\omega\varepsilon'$ is dominated by the permittivity term $\text{i}\omega\varepsilon'$. However, a linear growth of the phase with frequency is typical also of electromagnetic coupling. In particular, for the mutual inductance of the potential and current wires can be expressed as an imaginary impedance $Z_m^{\text{cable}} = \text{i}\omega M_{\text{cable}}$ (e.g. Fiandaca 2018).

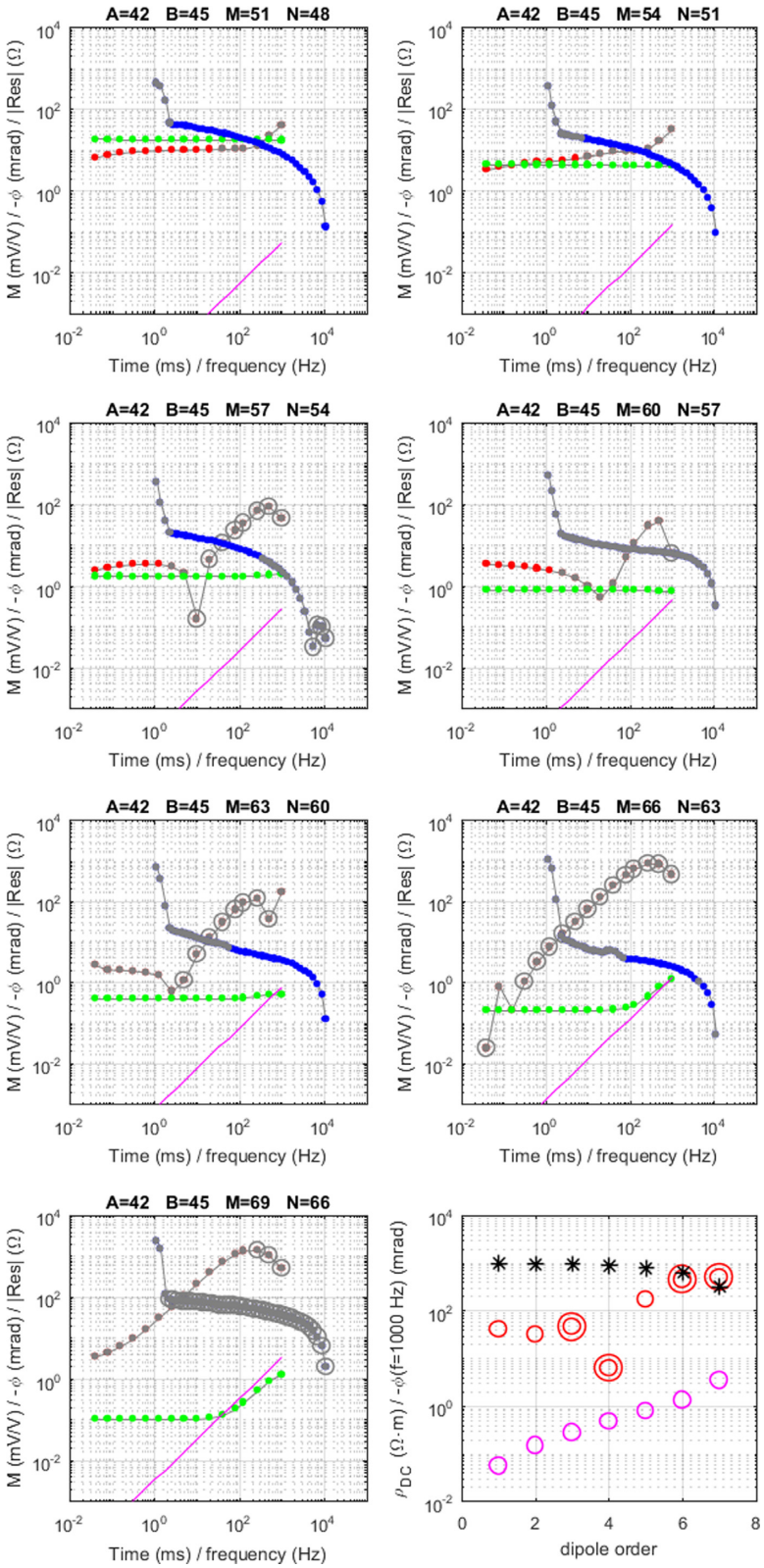

Figure A1. Example of dipole–dipole data (seven dipole orders for one AB dipole) for profile 1. Blue lines/markers: TD decays. Red lines/markers: FD phase spectra. Green lines/markers: FD resistance magnitude. Magenta lines/markers: phase of the EM FD induction for homogeneous half-space (ρ = measured ρ_a). Bottom-right panel: apparent resistivity (black stars), $f = 1000$ Hz EM induction phase (magenta markers) and measured phase (red markers) as a function of the dipole order. Greyed markers indicate data removed during processing. Circled markers indicate negative data.

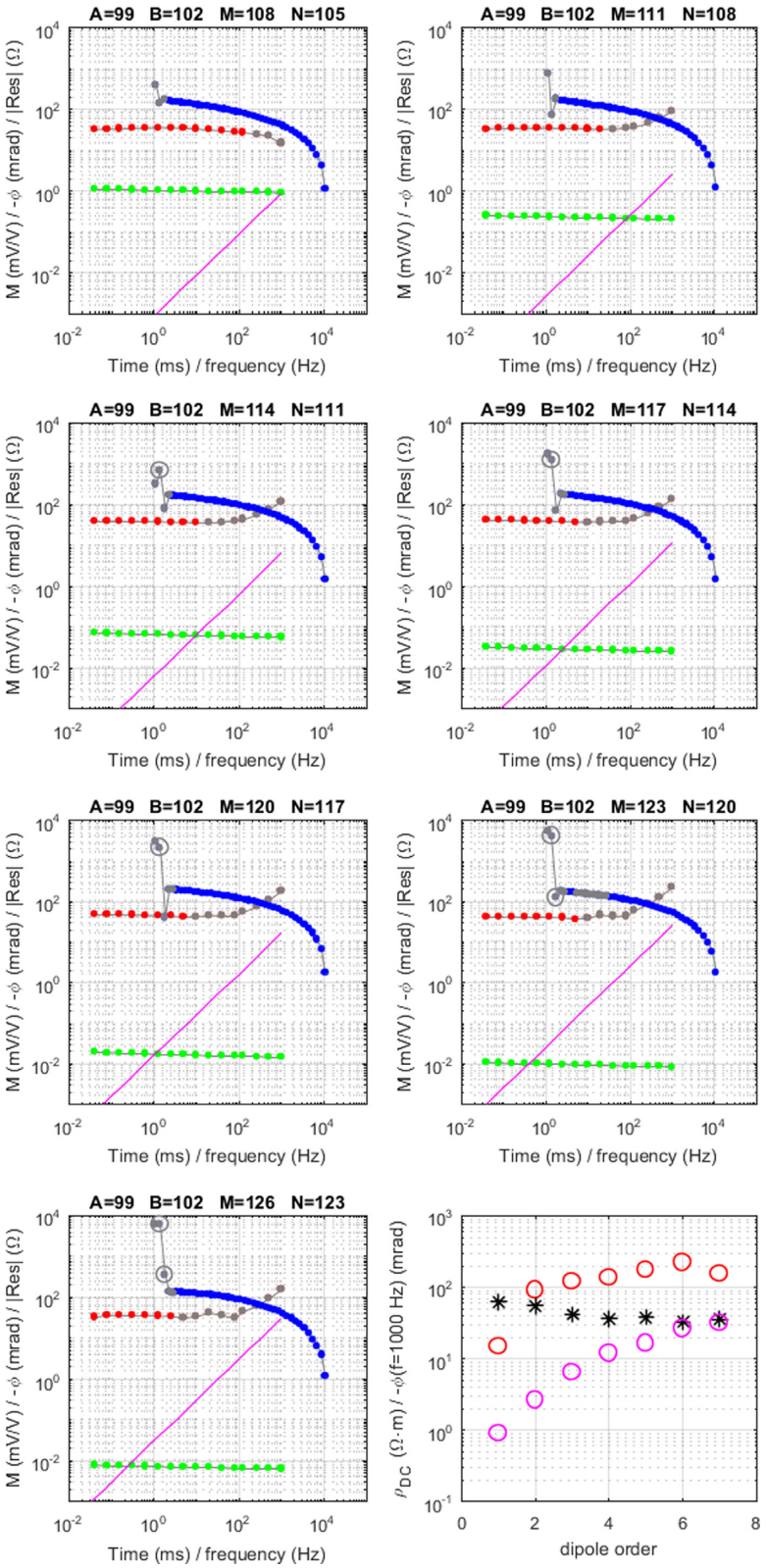

Figure A2. Example of dipole–dipole data (seven dipole orders for one AB dipole) for profile 2. Blue lines/markers: TD decays. Red lines/markers: FD phase spectra. Green lines/markers: FD resistance magnitude. Magenta lines/markers: phase of the EM FD induction for homogeneous half-space (ρ = measured ρa). Bottom-right panel: apparent resistivity (black stars), $f = 1000$ Hz EM induction phase (magenta markers) and measured phase (red markers) as a function of the dipole order. Greyed markers indicate data removed during processing. Circled markers indicate negative data.

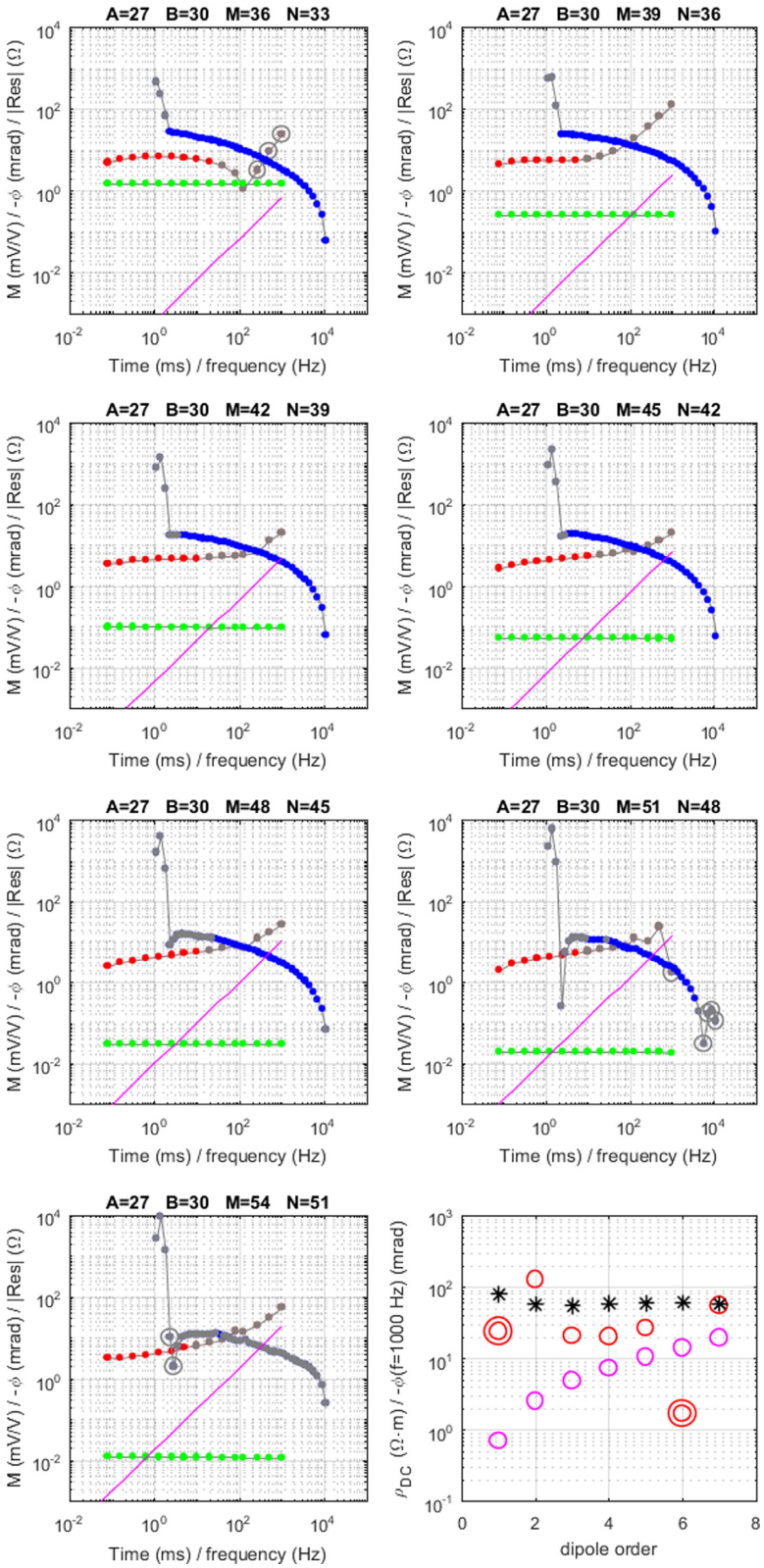

Figure A3. Example of dipole–dipole data (seven dipole orders for one AB dipole) for profile 3. Blue lines/markers: TD decays. Red lines/markers: FD phase spectra. Green lines/markers: FD resistance magnitude. Magenta lines/markers: phase of the EM FD induction for homogeneous half-space (ρ = measured ρa). Bottom-right panel: apparent resistivity (black stars), $f = 1000$ Hz EM induction phase (magenta markers) and measured phase (red markers) as a function of the dipole order. Greyed markers indicate data removed during processing. Circled markers indicate negative data.

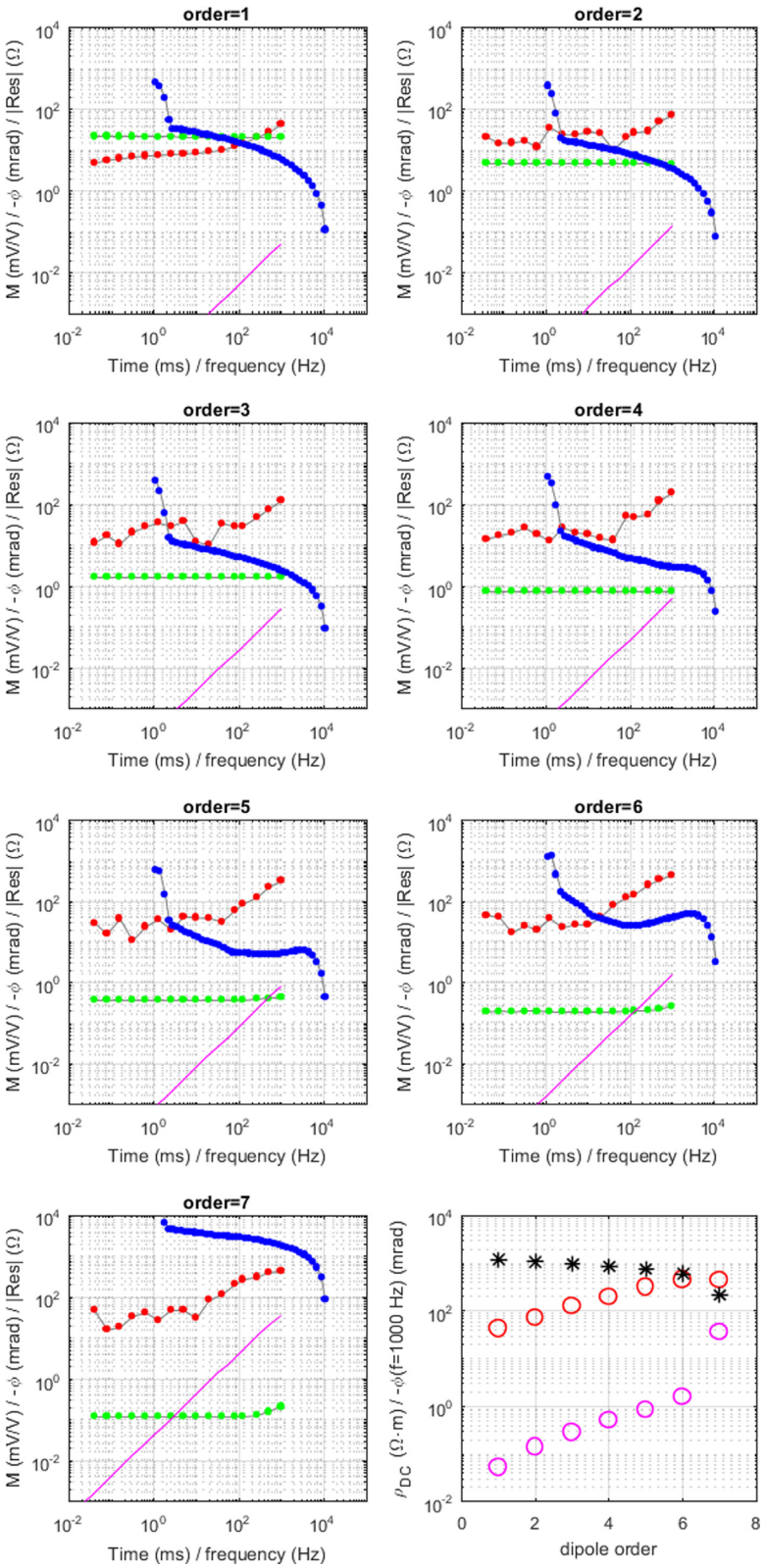

Figure A4. Average dipole–dipole data of profile 1. The average is carried out for FD phase spectra, EM induction phase and TD decays on all the dipoles of the profile (with AB = 3 m, on the absolute values). Blue lines/markers: TD decays. Red lines/markers: FD phase spectra. Green lines/markers: FD resistance magnitude. Magenta lines/markers: phase of the EM FD induction. Bottom-right panel: apparent resistivity (black stars), $f = 1000$ Hz EM induction phase (magenta markers) and measured phase (red markers) as a function of the dipole order.

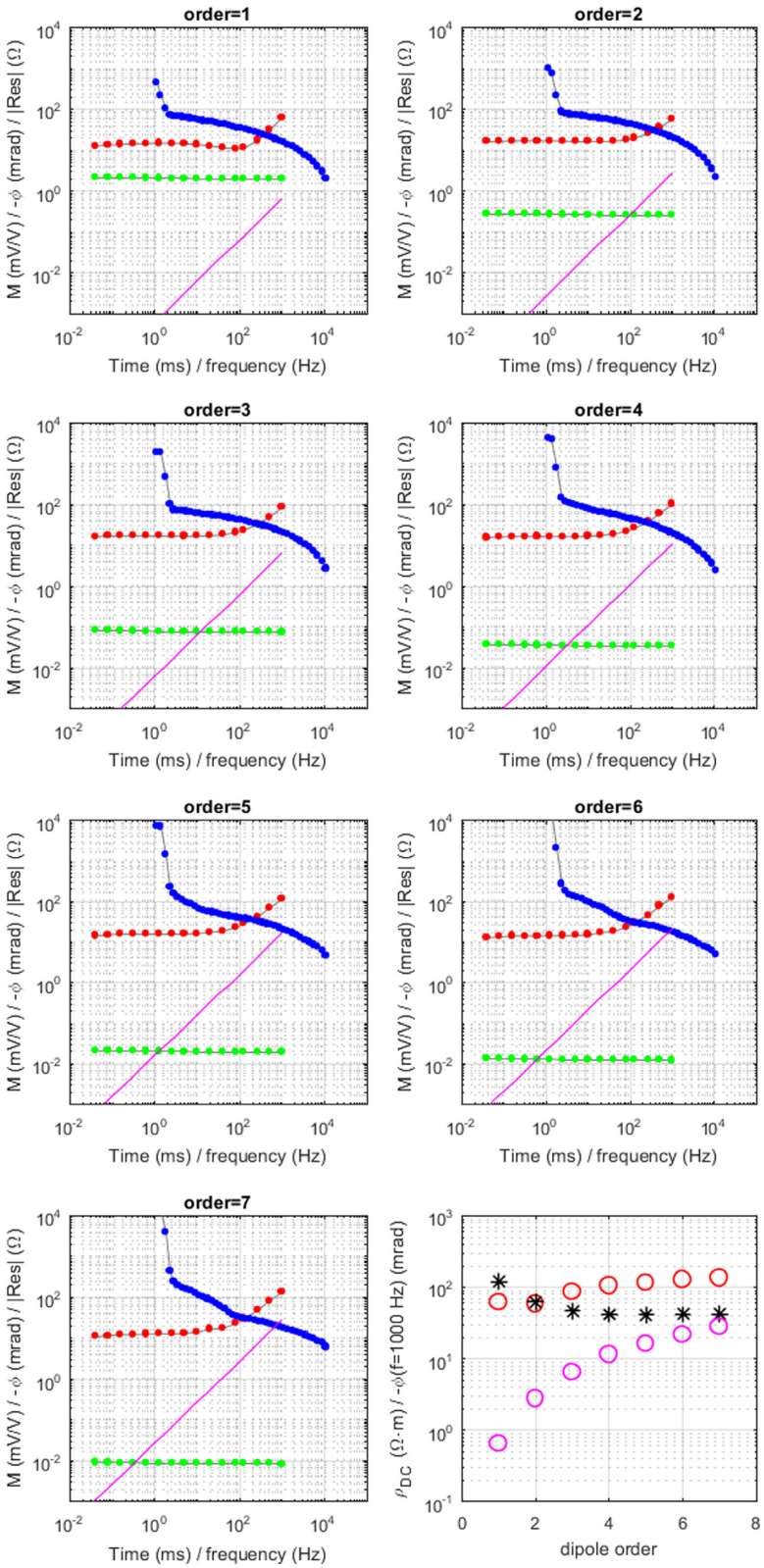

Figure A5. Average dipole–dipole data of profile 2. The average is carried out for FD phase spectra, EM induction phase and TD decays on all the dipoles of the profile (with AB = 3 m, on the absolute values). Blue lines/markers: TD decays. Red lines/markers: FD phase spectra. Green lines/markers: FD resistance magnitude. Magenta lines/markers: phase of the EM FD induction. Bottom-right panel: apparent resistivity (black stars), $f = 1000$ Hz EM induction phase (magenta markers) and measured phase (red markers) as a function of the dipole order.

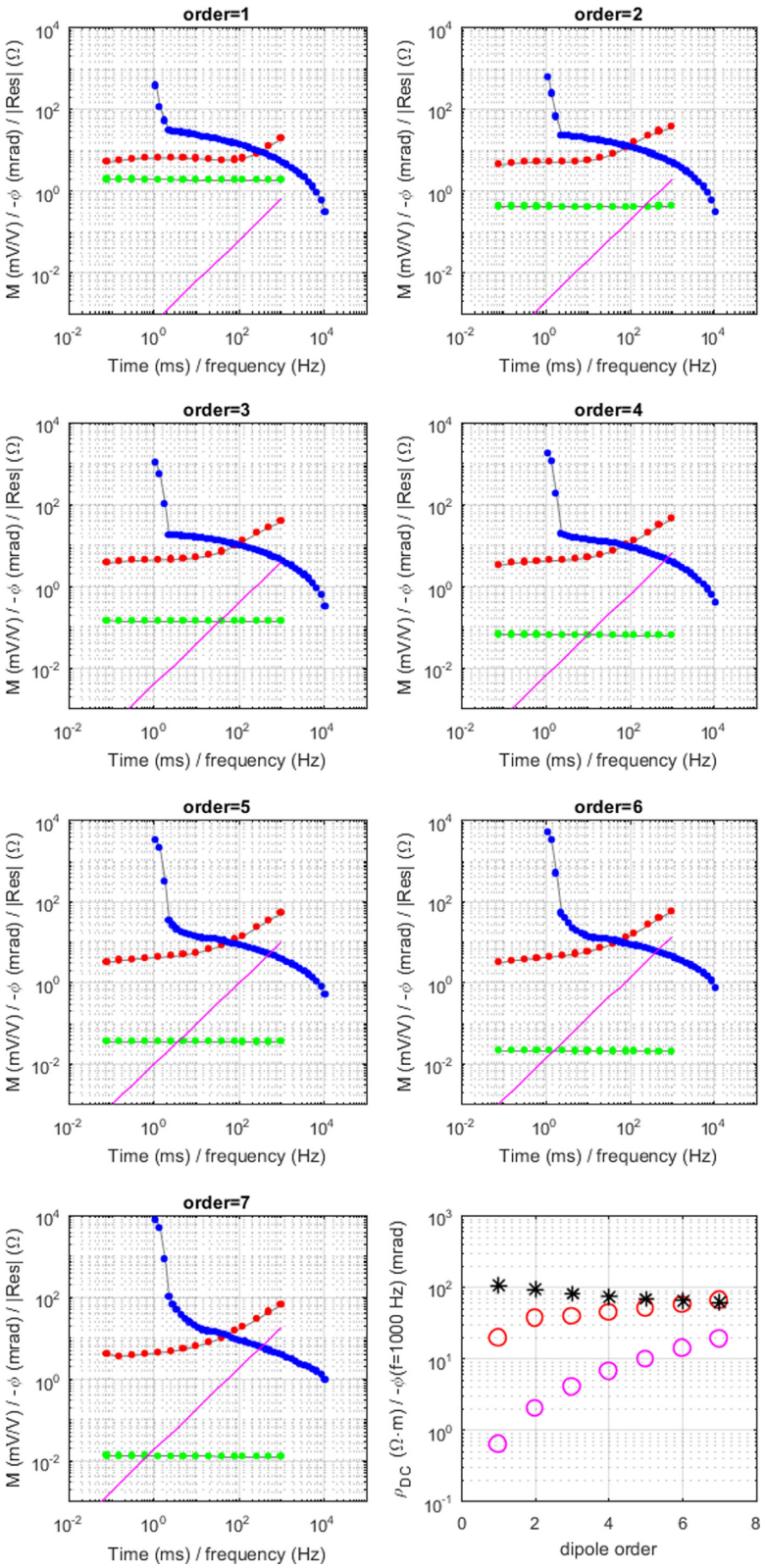

Figure A6. Average dipole–dipole data of profile 3. The average is carried out for FD phase spectra, EM induction phase and TD decays on all the dipoles of the profile (with AB = 3 m, on the absolute values). Blue lines/markers: TD decays. Red lines/markers: FD phase spectra. Green lines/markers: FD resistance magnitude. Magenta lines/markers: phase of the EM FD induction. Bottom-right panel: apparent resistivity (black stars), $f = 1000$ Hz EM induction phase (magenta markers) and measured phase (red markers) as a function of the dipole order.

Consequently, the high-frequency features of the measured spectra have two possible explanations, but the characteristics of the spectra and their changes when increasing the dipole order, together with the knowledge of the geology of the sites, might help in interpreting the spectra features.

Figs A1–A6 present the acquired dipole–dipole data for the three profiles, as a function of the dipole order. In particular, Fig. A1 shows an example of dipole–dipole data for a specific AB injection of profile 1 (at Grindsted), with a panel for each dipole order (up to order 7). Together with the phase spectra, Fig. A1 presents the absolute value of the measured resistance (in green), the corresponding TD decays (in blue) and the phase of the EM induction (magenta lines), computed following Sunde (1968) for the homogeneous half-space with resistivity equal to the measured apparent resistivity (and without considering IP effects). The data rejected during the manual processing are shown in grey. In the bottom-right panel in Fig. A1, three types of data are shown as a function of the dipole order: the measured apparent resistivity (black stars); the measured phase values at the highest frequency ($f = 1000$ Hz); the computed phase values of the EM induction at the highest frequency ($f = 1000$ Hz). Figs A2 and A3 show the same type of data for selected dipoles of profiles 2 and 3, respectively (i.e. the Samsoe profiles measured at the landfill and near the landfill).

In Fig. A4 the average data of the FD phase and amplitude spectra, TD decays and FD EM induction phase spectra are presented. The average values are computed for all the quadrupoles of the profile with same dipole order (taking the absolute value of the phase and decay data for avoiding signal cancellation when the data change sign from one quadrupole to the other). Figs A5 and A6 present the same type of data for profiles 2 and 3, respectively. Generally, the trends shown in Figs A1–A3 are reflected in the trends of the average signals: the phase increases with frequency and dipole order is a common features on all current injections for the three profiles. Furthermore, for profile 1 an increase of the magnitude with frequency is also present for high dipole orders.

Overall, the high-frequency behaviour of the FD phase spectra with the dipole order is really similar to the induction behaviour, even if the signal level of the measured phase is always higher than the computed EM induction. There are three possible explanations for this:

(1) The measured high-frequency phase spectra, with increasing phase more pronounced for high dipole-order values, are due to the geology at the sites, for instance because of an increasing clay content with depth, and not to the EM coupling.

(2) The estimate of the EM effects using a homogeneous half-space model, and neglecting the capacitive coupling, underestimates the total EM coupling.

(3) The high-frequency features of the measured spectra are due to both geology and EM effects.

The first hypothesis relies on the fact that some lithologies more than others present a significant increase of imaginary conductivity with frequency. In particular, clay materials often present a continuously increasing imaginary conductivity, with Maxwell–Wagner polarization (i.e. dielectric polarization) dominating at high frequencies (Leroy & Revil 2009). Actually, two thin lignite layers (approximately 1 m thick) are present at 10 and 30 m depths along profile 1, which is otherwise dominated by sand deposits. But in Fig. A1 the significant increase of high-frequency phase values with dipole order is not followed by a corresponding decrease of the apparent resistivity: the apparent resistivity is almost constant, except for a sharp drop for order 7. In Fig. A4, where the order-by-order average of all the signals along profile 1 is considered, the average apparent resistivity slightly decreases with dipole order, again with a more pronounced resistivity decrease at order 7, but the increase of high-frequency phase is much more pronounced. Furthermore, it has to be considered that along profile 1, below the shallower lignite layer, a highly conductive contaminated plume exists, which influences the resistivity structure more than the lignite layer itself. The conductive plume in any case is far from the source zone, and the contaminant concentrations are well below the concentrations which originate IP effects (e.g. above 1 g l^{-1} for BTEX in Orozco *et al.* (2012)). More importantly, both in Figs A1 and A4 a significant increase of the magnitude of the resistance is evident for high dipole orders: this feature is not compatible with IP effects for which the resistance magnitude decreases with frequency (e.g. Fiandaca *et al.* 2018). The clay argument cannot be applied for profile 2, at least in the south area of the profile where the landfill is present (and where the example AB current dipole is taken in Fig. A2). This is not a conclusive argument because we have no knowledge of the spectral characteristics of the landfill materials. In any case the average signals of Fig. A5, which reflect both the areas above the landfill and outside the landfill, present features similar to the exemplar current dipole of Fig. A2. Along profile 3 the geology is characterized by a top silty sand layer (3.1 m thick), followed by a thin clay/till layer (0.9 m thick), a sand layer (4.3 m thick), a thick clay/till layer (15.6 m thick) and a sand layer (down to at least 30 m). Consequently, the geology is not as simple as along profile 1. Nevertheless, similarly to Fig. A1, in Fig. A3 the constant increase of high-frequency phase with dipole order is not accompanied by a corresponding decrease of resistivity, which is practically constant after the first dipole order. Similarly to Fig. A4, in Fig. A6 a small decrease of average apparent resistivity with dipole order is present, but again the increase of high-frequency phase is much more pronounced.

The second hypothesis about the mismatch between the high-frequency measured spectra and the computed EM effects is that the EM effects are underestimated. Actually, Dey & Morrison (1973) show that for a two-layer model with a conductive layer below a resistive top layer the EM induction is significantly higher than the induction of a homogeneous half-space with resistivity equal to the top layer. Especially in profiles 1 and 2 the inverted resistivity models present a conductive layer below the top resistive layer. This explanation might be valid despite the small variations of apparent resistivity with dipole order because the EM fields sense differently the resistivity distribution, with more weight on the conductors in comparison to the DC apparent resistivity. Furthermore, the capacitive coupling between the potential wire and the ground is not considered in the EM computation presented in Figs A1–A6. Ingeman-Nielsen (2006) shows that the capacitive coupling can have a severe effect on the FD measurements, and that the capacitive coupling increases with the contact resistance and the dipole length, but decreases with the dipole order. This means that the capacitive coupling should be more pronounced for low dipole-order values, and may explain the bigger difference evidenced in the figures between the measured high-frequency phase values and the computed EM induction for low dipole orders. All these are indications that our computations underestimate the EM coupling, but a full EM solution of the forward problem, including the capacitive coupling, would be necessary for a proper modelling and quantification of the EM effects. This is done for instance in 1-D by Ingeman-Nielsen (2006), but a full EM solution of the forward mapping is beyond the scope of this study.

The third hypothesis is that lithologies characterized by a significant increase of imaginary conductivity with frequency are present at the sites, but that significant EM coupling affects the measured data. This could explain the difference in magnitude between the measured phase spectra and the computed EM effects, partially or entirely, especially for the low dipole orders for which the trends of the measured phase and the EM induction are more different.

In conclusion, the overall behaviour of the phase increase with dipole order is very similar on the three profiles and reflects trends comparable to the EM induction computed on homogeneous half-spaces, regardless of the differences of the geology along the three profiles. Furthermore, there is a lack of correlation between the trends of measured apparent resistivity and high-frequency measured phase, and on profile 1 the increase of resistance magnitude is not compatible with dielectric-like polarization. This lets us believe that the measured spectra are severely affected by EM coupling, and that only the second and third hypotheses are compatible with the measured data. Consequently, in the absence of a full EM solution of the forward mapping, we retain that it is difficult to safely interpret the phase data with spectral trends resembling the EM induction and, consequently, we cull out these data before inversion. The same reasoning applies to the TD decays for which the early-time data characterized by an abrupt change of slope are removed during the processing.